Chapter 1.   Introduction and Motivation

1-1   Motivation

Nanocrystalline TiO_2 and ZrO_2 have attracted great attention on solar energy,[1] gas sensor,[2] photocatalysis,[3] and super solid acid catalyst.[4]   Moreover, $ZrTiO_2$ binary metal oxides or solid solution have shown higher efficiency for degradation of organic compounds than pure metal oxides.[2,5,6]   Therefore, much effort has devoted to improve the photoactivity of the metal oxides in terms of developing promising preparation method and studying the physicochemical properties with the respect to the preparation conditions.   Thermal treatment is an essential process for most materials prepared by chemical synthesis because of crystallization.   Moreover, calcination history has been demonstrated to greatly control their physicochemical properties including crystalline structure, surface chemical composition, band gap, and surface area.[7]   Stone and Davis have used dodecyl phosphate as a directing agent for the preparation of mesoporous TiO_2 and removed the templates through calcination.[8]   In addition, phosphate species was incorporation into the surface lattice of TiO_2 after the thermal treatment.   The surface phosphate species decreases the photoactivities of TiO_2 and the authors attribute the low photoactivies to high concentration of phosphor-derived defects.   Modification with phosphate species on TiO_2 is reported to enhance the thermal stability of anatase form and porous structure,[9] surface acidity and photoactivities.[2]   Moreover, the content of phosphorous also effects the photocatalytic reactions and the optimal concentration of phosphorous is 1.4 wt %.[10]

Non-hydrolytic sol-gel (NHSG) method provides a kinetically lower rate than hydrolytic sol-gel method that allows the preparation of homogeneous gels.[11,12]   Therefore, the preparation process can more effectively control the growth of gels.   Moreover, the use of trioctylphosphine oxide (TOPO) molecules as chelating agents via nonhydrolytic sol-gel

process gives a convenient approach for synthesis of TiO_2 and ZrO_2 nano-crystalline particles.[13,14] Chang and Doong have prepared TOPO-capped $Zr_xTi_{1-x}O_2$ nano-crystals via NHSG route and demonstrated that the TOPO-capped $Zr_{0.03}Ti_{0.97}O_2$ had highest photoactivity toward the degradation of RhB dyes.[15] Organic TOPO is a kind of phosphorous-containing surfactant. Therefore, phosphated TiO_2 could be obtained after calcination of the TOPO-capped nanocrystals in air. However, calcination effect on physicochemical properties as well as the photoactivity of the TOPO-capped Zr^{4+}/TiO_2 has not been addressed yet.

1-2 Objectives

This research aims to investigate the physicochemical properties of TOPO-capped Zr^{4+}/TiO_2 nano-crystal calcined at elevated temperatures in air by means of thermo-gravimetric analysis/differential scanning calorimetry (TGA/DSC), X-ray photoelectron spectroscopy (XPS), X-ray powder diffractometry, high resolution transmission electronic microscope (HRTEM), fourier-transform infrared spectrometer (FT-IR), UV/vis spectrometry (UV-vis), inductively coupled plasma mass spectrometry (ICP-MS), nitrogen adsorption-desorption BET model and dynamic light scattering. Decoloration sof RhB by the calcined $TiO_{2,}$ as-prepared sample and Degussa P25 were also determined to understand the effect of calcinations on the photoactivites of the nanocrystals. Moreover, the photoactivities of the TOPO-capped nanocrystals regarding to their physicochemical properties are elucidated.

Chapter 2.   Background and theory

2-1   TiO$_2$ semiconductor photocatalysts

2-1-1   Material properties

Both semiconductor and insulators have energy barriers of band gap for electric movement which is dissimilar with the conductors with continuous electronic state.   Band gap is the void region which ranges from the top of the filled valence band to the bottom of the vacant conduction band.   Semiconductor is different from insulators mainly on the scale of band gap energy.   Large band gap scale between valence band and conduction band of insulator prevents electrons within valence band reaching conductions band. Semiconductors have appropriate band gap scale for electrons to cross the void region as long as enough energy is obtained.   Generally, many semiconductors can be excited by energy in terms of heat or photo.[16]   The excited semiconductor has electron and hole pairs within conduction band and valence band, respectively for further redox reactions.[16]

TiO$_2$ is one of the semiconductor materials which has three types of crystalline structure: anatase, rutile and brukite.   With the increase of energy, amorphous TiO$_2$ first turns to metastable anatase form and followed by more stable form of rutile.   The phase transformation from anatase to rutile is at about 500 °C which depends on the preparation method and precursors.   Because of anatase TiO$_2$ has suitable band gap energy of 3.2 eV, redox potential and photoactivity for applications; anatase has been widely used in many aspects.

Band energy positions and the redox potential of semiconductors determine the ability of photo-induced charges to transfer to acceptors.   Induced electrons within conduction band are ready for relaxation to valence band or transfer to acceptors for reduction reaction.

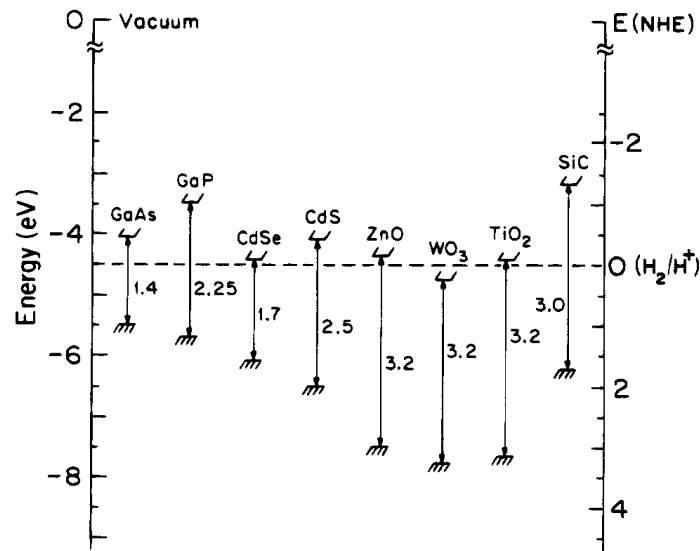Additionally, induced hole within valence band can also accept electrons from donors.

Figure 2-1.　Energies for various semiconductors in aqueous electrolytes at pH = 1.[16]
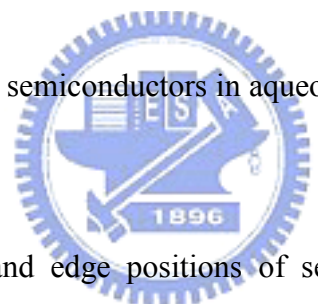
Figure 2-1 displays the band edge positions of several semiconductors.　Left axis presents the internal energy scale relative to the vacuum level and on the right for comparison to normal hydrogen electrode (NHE).　The positions are originated from the flat band potentials in a contact solution of aqueous electrolyte at pH = 1.　The pH of the electrolyte solution influences the band edge positions of the various semiconductors compared to the redox potentials for the adsorbate. For TiO_2, it has band gap around -0.3V to +2.9V.

Recently many groups are curious about nano-scaled TiO_2, especially for nanorods, nanotube, and nanoparticles.[17]　They have potential properties very different from bulk ones. The most apparent change is quantum size effect that total atomic numbers decreases with the decreases of particle size.　As a result, the energy levels within solids are reduced. Shrinkage of the original energy bands results in the expanding of extension from top of valence band to bottom of conduction band.

2-1-2   Applications on decomposition of environmental pollutants

Light is used as energy source for photocatalysts to excite charge carries for redox reactions.   Once the electrons and holes are generated by enough energy, several pathways may happen[16].   As presented in Figure 2-2, the induced charges diffuse to surface or inside of bulk phase and recombine with release of energy.   Surface charges would reduce and oxidize the adsorbed-compounds by electrons and holes respectively.   For oxidization and reduction, electron would transfer from higher energy level (donor) to lower one (acceptor) as contacting to each other.
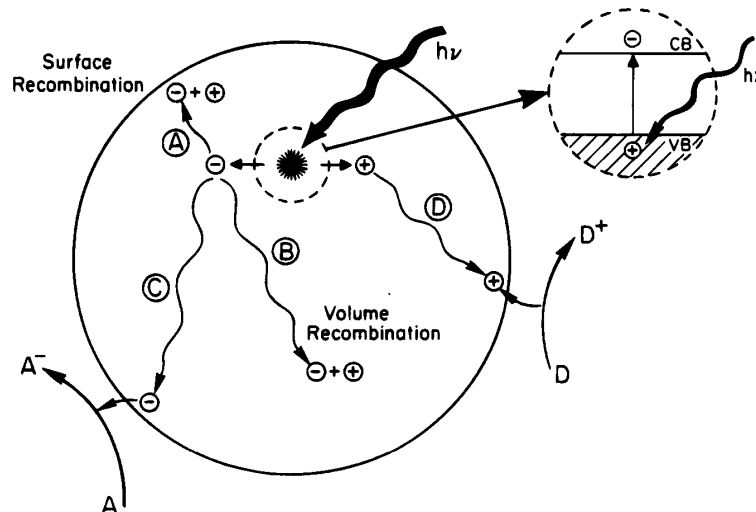

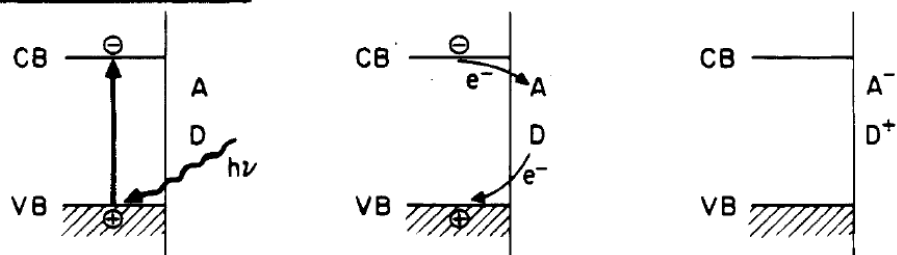Figure 2-2.   Induced charge currieries undergo recombination and electron transfer.[16]

Figure 2-3.   Electrons transfer from higher energy level to lower one.[16]

Hydroxyl radicals, which have high oxidizing ability, are usually produced in hydrolytic solution for advanced oxidation process (AOP) process in decomposition of organic compounds. In conventional AOP process, Fe^{+2}/H_2O_2, catalysts/O_3 and UV/H_2O_2 are acting for hydroxyl radicals producing. Nowadays, TiO_2 has potential properties, like electronic potential energy, band gap energy, chemical stability, nontoxicity and low cost for inducing charge carriers with variable approaches. Dispersed in water and irradiation by UV light, electron/hole pairs are introduced and diffuse to surface for redox reaction.[18] Oxygen and water molecule reacts with electron and hole respectively; result in the final product, hydroxyl radicals (Figure 2-4).[18] Induced hydroxyl radicals are ready to react with and oxidize compounds in solution. Minimization of organic compounds was expected to be caused by introduced-hydroxyl radicals or directly reacted by electron/hole pairs on surface of photocatalysts.

$$e^- + {}^\bullet OOH + H^+ \rightarrow H_2O_2 \qquad \text{(formation of } H_2O_2\text{)}$$

$$H_2O_2 + e^- \rightarrow {}^\bullet OH + OH^- \qquad \text{(formation of } {}^\bullet OH \text{ radicals)}$$
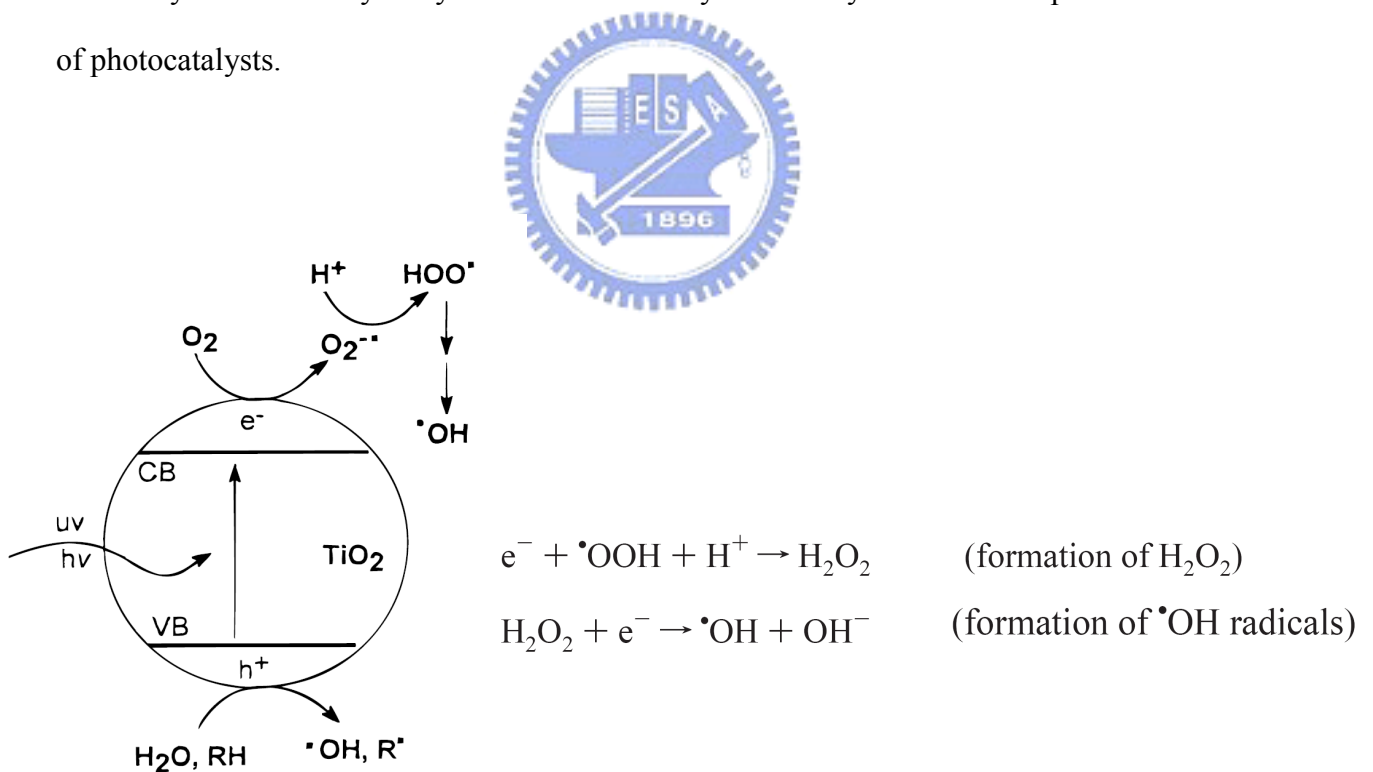
Figure 2-4. Photo-induced charge carriers and their transfer.[18]

2-2 Surface modification

Though TiO$_2$ is one of the most well-known semiconductors performed for widely applications, many researches on modification of TiO$_2$ such as doping impurities, coating with organic or inorganic compounds, and compositing with other semiconductors were published.[2,19] Modified TiO$_2$ is dissimilar to the pure one on several aspects, such as absorption capacity, optical response, charge recombination rate and interfacial charge transfer kinetics. Table 2-1 lists the functions of some modifiers used on TiO$_2$ or other photocatalysts. The approach of modification can give wider uses and enhance activity of semiconductors and even improve some disadvantages for practical applications.

2-2-1 Modification with metals

Several novel metals and transition metals (Ni, Cu, Pt and Ag .etc) have been used for catalysts on reduction of NOx and oxidation of volatile organic compound (VOC) without combining with semiconductors.[2,20-22] Some physicochemialc properties of metals and semiconductors are different and the contact of these two materials can induce some effects at the interface. Schottky barrier occurs at surface state once semiconductor contacting to metals due to their difference of work function. Work function is defined as energy required for electron escape from Fermi level to vacuum level (energy is 0 eV). Electron redistribution within interface of metal and semiconductor takes place when electrons at higher electron potential levels flow to lower one for final equilibrium. Figure 2-5 displays the formation of Schottky barrier at interface between novel metal (Pt as example) and TiO$_2$. Table 2-2 lists work functions of some metals and most of them are (Pt = 5.65 eV) higher than that of TiO$_2$ (4.1 eV) so that TiO$_2$ has higher energy of Fermi level.[23] In Figure 2-5, electrons move from Fermi level of TiO$_2$ to that of Pt and the electrons redistribution occurs between Pt and TiO$_2$ until the energy at interface is constant. In order to maintain the

equilibrium between Pt and TiO_2, some electrons from TiO_2 are trapped at interface. The formation of electron redistribution by the difference of work functions of TiO_2 and Pt is denoted as Schottky barrier. Schottky barrier height is equal to the difference of TiO_2 and other metals ($\Phi_m - \Phi_{TiO2}$). This barrier can trap electron at interface and prevent it flowing back to TiO_2. Electrons accumulate at interface can further transfer to substrate for oxidation or reduction reaction. Once the composite is irradiated by UV light, the induced electrons can trapped at interface contributed to reduce the recombination rate.

Loading of metals also plays an important role that optimal weight percent is required for better activity.[22] Sun et al. presented that 1 wt% of platinum on surface of HK UV100 anatase form TiO_2 shown higher photocatalytic decomposition of phenol on the basis of concept of Schottky barrier between Pt and TiO_2. They introduced a possible equilibrium between charges' trapping, recombination and creation inside unmodified anatase. Once when Pt contacts with TiO_2, some excited electrons were trapped at interface and the equilibrium was broken. Since the electron density inside TiO_2 decreases with the increase of trapping electrons, recombination of electrons and holes also decreases. However, due to the increase of trapping electrons at interface by increase of Pt, the electronic potential gradient within TiO_2 would decrease which result in the decrease of electronic flux through interface. Therefore, the recombination rate inside TiO_2 increases contrarily.

Table 2-1.　Function of modifier and the placations.

| Surface enhancement	Ref.
1.　Adsorption	[24]
2.　Charge scavenger: acid / basic sites, unsaturated coordination of Ti, TFA (electron withdraw)	[2]
3.　Schottky barrier (novel metals: Ag, Au, Pt, Pd)	[16,22]
4.　Enhancement on surface area	[24]
5.　Surface defect site: trapping agent	[2]
6.　Surface sensitization	[25]
Structure aspects	
1.　Prevent pore shrinkage by annealing(phosphate/ carbon)	[24]
2.　Prevent phase transformation (carbon/ phosphate)	[2]
3.　Semiconductor binary: over lap of electronic energy levels	[26,27]
4.　Surface sensitized: absorption of visible light	[26,27]
5.　Surface acidity: phosphate, triflouroacetate acid, acetate.	[2]
6.　Semiconductors: WO_3, V_2O_5, PbS	[20,27]
7.　Novel/transition metals: Au, Pt, Pd, Ag	[16,28]
8.　Support: Al_2O_3, SiO_2, activated carbon, zeolite	[19,29]
Applications	
1.　solar cell	[27,30]
2.　hydrogen production	[6]
3.　water and air purification	[2,16,22]
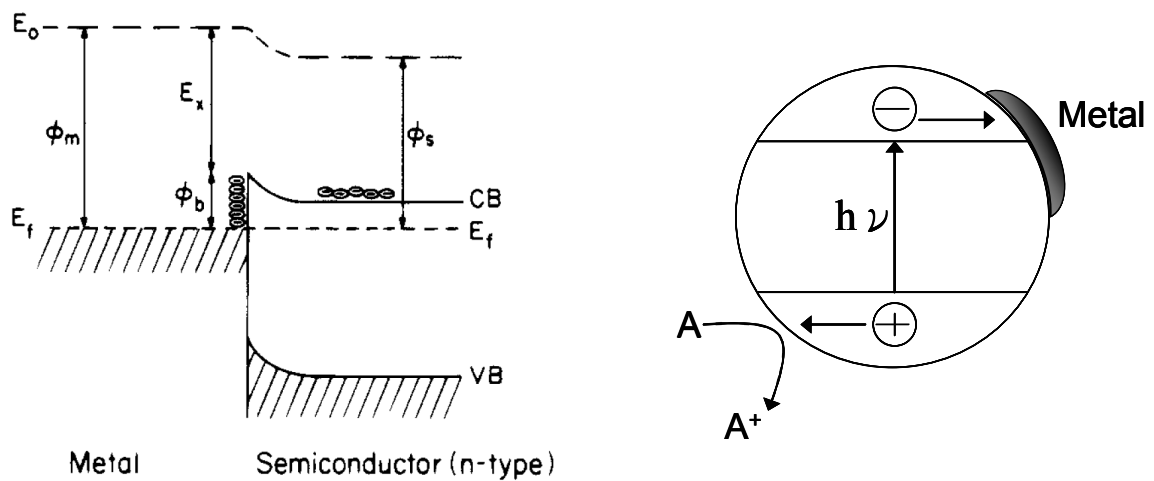
Figure 2-5.   Schottky barrier formation and separation of induce charge cariers.[16]

Table 2-2.   Work functions of metals.

Metal	Mg	Al	Ca	Ti	Cr	Fe	Co	Ni	Cu	Ga
Φ_m eV	3.66	4.28	2.87	4.33	4.5	4.5	5.0	5.15	4.65	4.2
Metal	Mo	Pd	Ag	In	Sn	Ba	Ta	W	Pt	Au
Φ_m eV	4.6	5.12	4.26	4.12	4.42	2.7	4.25	4.55	5.65	5.1

2-2-2   Modification with dopants

Impurities other than titanium were mostly used to dope into crystalline structure of TiO$_2$ to vary some physicochemical properties of original TiO$_2$.   Transition metals such as W, V, Ce, Zr, Fe, and Cu metal ions were introduced to replace Ti^{4+} for introduce of an additional energy level.   Much researches demonstrated that introduce of metal ions can make TiO$_2$ response to light with longer wavelength.   The absorption edge shifted to visible light is more practical for application by irradiation of solar energy.   Because of an

additional energy level introduced within conduction band and valence band of TiO_2, the excited electrons at conduction band can first relax to the additional energy level and then drop to valence band. The additional energy level has proved to reduce the recombination rate of electrons and holes which was observed with longer lifetime for relaxation.[26]

In addition to optical response, the acidity of doped TiO_2 was also varied by different species and concentration of metal ions. However, literatures have illustrated that the acidity of doped-TiO_2 was adjustable by incorporation of metal ions.[31] Surface acidity of solid catalysts has been well recognized as an important role on the reaction mechanism, selectivity, and efficiency.[21]

For practical applications, not only the exciting energy but also the stability is under considered. Substitutes of impurities to the lattice point of TiO_2 strengthen the stability of anatase structure of TiO_2. Guidi et al. claimed that dopants such as La and Nb have been proved effective to prevent grain coalescence and maintain the anatase crystalline structure.[32]

Impurity like Zr^{4+} has also been used to enhance stability and structure strain force of TiO_2. Yang et al. reported that the incorporation of Zr^{4+} within structure of TiO_2 has successfully maintained anatase form until 900 °C on the basis of XRD patterns.[33] Moreover, Chang et al. has published that $Zr_{0.03}Ti_{0.97}O_2$ shown higher rate of RhB decoloration than pure TiO_2 did because of proper defects induced by Zr^{4+} ions.[15]

In addition to metal ions, some non-metal ions were also demonstrated as effective impurity incorporated into structure of TiO_2. They were proved to shift the optical response of TiO_2 to visible light, reduce the recombination rate and enhance the thermal stability.

Nitrogen has been widely used for dope and been illustrated with well response to visible light for excitation of electrons.[34] Cong et al. also observed Ti-O-N and O-Ti-N bonding as evidence of the source of additional energy level between valence band and conduction band.[34] The insertion of energy level can not only shift light absorption to visible region but also can trap induced electrons for lower recombination rate.

Whether using metal or non-metal ions as dopants, the content of dopants also influences a lot for better photoactalytic efficiency. The optimal concentration of dopants for better photoactivity is always related to the species of dopants, method for preparation, and the structure of different metal oxides.

2-2-3　Modification with semiconductors

Composite semiconductors display special properties for increase of efficiency, based on the relative conduction band and valence bad position. Relative band energy positions of each semiconductor play a critical role on the arrangement of energy bands. Figure 2-6 displays a sandwich-like arrangement of band gap energy positions from the binary semiconductors as an example. Semiconductors with shorter band gap would be excited by longer wavelength like visible light. The induced electrons transfer from higher conduction band to the lower one and the holes still stay in the higher valance band. Therefore, the excited charge carriers are separated with larger distance and the recombination rate will decrease. The separation of electrons and holes has been used in solar cell and photocatalysts for higher photon-efficiency under solar light irradiation. The use of binary semiconductors also exhibits a wider scale of redox potential when both semiconductors are excited. The larger the redox potential is the higher reactivity scale will be.[20] Ling Wu used CdS couped with TiO_2 which exhibited higher oxidation of methylene blue in water or nitric oxide in air under visible light irradiation.[20]
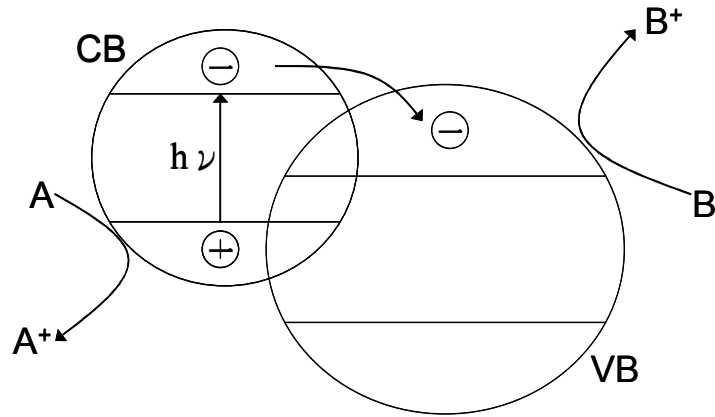
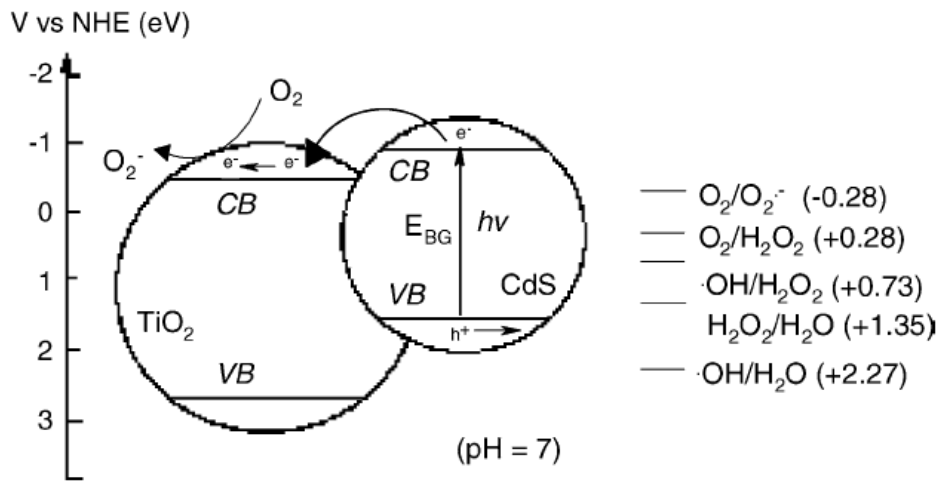Figure 2-6.   Binary of semiconductors with specific band energy positions.[20]

Figure 2-7.   Redox potentials of the valence and conduction bands of CdS sensitized TiO_2

nanoparticles and various redox processes occurring on their surface at pH 7.[20]

2-2-4 Modification with organic compounds

Several researches have presented that modification with organic compounds and post-heat treatment provides catalysts higher activity and special functions. Structure directing agents like cationic, anionic surfactants and block copolymers and the succeeding removal process also afford certain influence on photoactivity.[35,36]

Activated carbon is a promisingly material for adsorption of organic compounds via high surface area. In order to prolong the lifetime of activated carbon, photocatalysts like TiO_2 has been combined on it for degradation of organic pollutant.[37] On the other way, composite of activated carbon and photocatalysts can enhance the photodegradation rate through the pre-adsorption of organic compounds by activated carbon. Thus, many researches have contributed to enhance the application of adsorption and degradation by composite of AC/TiO_2.[38]

In order to concentrate more organic compounds near TiO_2, Nagaoka et al. have prepared spherical carbon and cellulose microspheres doped with TiO_2 nano-particles on the surface.[39] They have observed that the carbon/TiO_2 can remove acetaldehyde without light irradiation indicating that the carbon around TiO_2 effectively adsorbed target compounds. Though pure TiO_2 presented degradation of acetaldehyde, carbon/TiO_2 had even higher efficiency for removing of target compounds.

Sangaraju and co-workers have report a $TiO_2@C$ core-shell like materials prepared by direct heating of Ti(IV) oxyacetyl acetonate within closed vessel call.[24] The outer shell carbon can not only inhibits agglomeration and growth between TiO_2 particulates but also enhances the thermostability without phase transformation.

Composite with carbon still led to some drawbacks that lower the photoactivity: the carbon layer decreased the intensity of incident light for exciting charge carriers, the adsorbed compounds had to diffuse through carbon layer to the active surface of TiO_2 for further reaction.[38,40] The adsorption behaviors and the subsequent oxidation were both influenced

by the content of carbon and TiO_2. TiO_2 occupied the adsorbing sites of carbons and high content of carbons also suppress the transfer of compounds for reaction.

With strong electron-withdraw ability, Jimmy C. Yu. used trifluoroacetic acid to modify TiO_2 thin films by dipping TiO_2-coated glass slide into TFA solution and post heating at 250°C for chemisorption.[2]   Photoluminescence spectra indicated that photogenerated electrons at Ti^{+3} was attracted by the most electronegative element, fluorine, of the modified samples and showed lower photoluminescence intensity than unmodified ones.   Although the modified samples heat-treated at 250 °C have higher photocatalytic oxidation of acetone than the others, the degradation rate decreased with the decomposition of chemisorbed TFA during irradiation.
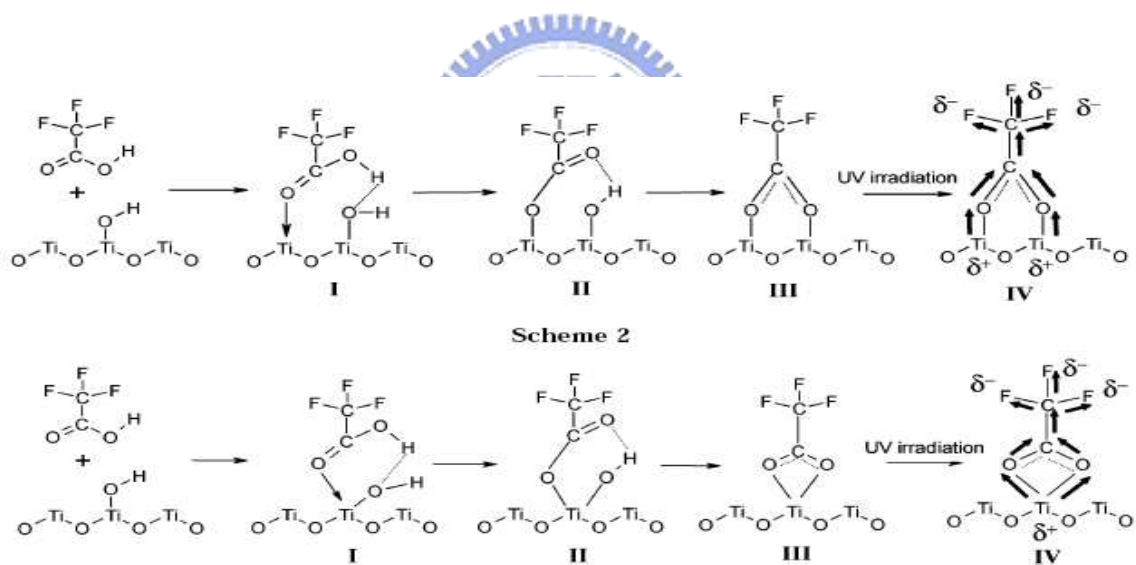

Figure 2-8.   Scheme of chemisorbed TFA on TiO_2 and the electron transfer behavior during irradiation.[2]

Vitamin C (ascorbic acid) has been used as modifier chemisorbed on TiO_2 surface by the chelating of electrons from ascorbic acid to surface Ti^{4+} ions.[25,41] The role of ascorbic acid is similar to the dye for sensitization of visible light absorption from solar light. Figure 2-5 displays the transfer of photogenerated electrons from ascorbic acid to TiO_2. Ascorbic acid donates the excited electrons to the conduction band of TiO_2 by adsorbing solar energy. Wei Liao has successfully used ascorbic acid for photodegradation of azo dye with solar light irradiation.[25] The disadvantage of using organic compounds as modifiers for catalysis is the decomposition of modifiers under oxidizing environment by light irradiation and the modification for photocatalysis is only temporary.
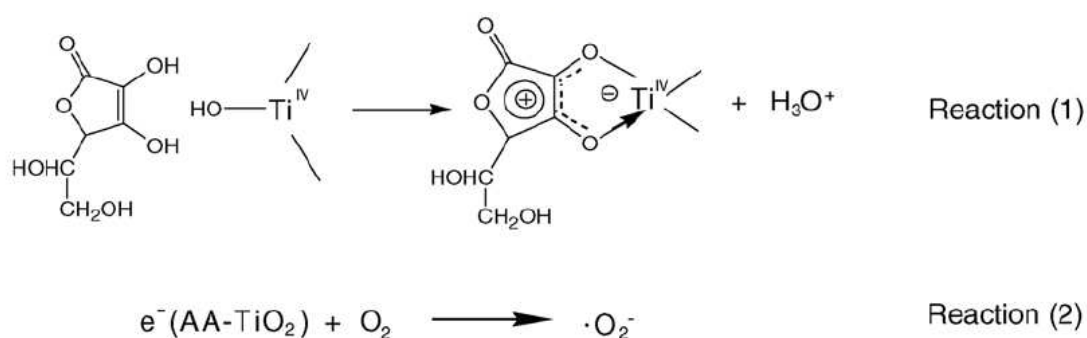

Reaction (1)

Reaction (2)

Figure 2-9. Scheme of interaction between Vitamin C and surface Ti^{4+} ion and the induced-electron transfer from Vitamin C to Ti^{4+}.[25]

Stabilizing agents can suppress the growth of grains and control the particle size by chelating to the condensation sites during sol-gel preparation process. Many semiconductors significantly affected by particle size in physicochemical properties. Size-effect apparently occurs on band gap energy of semiconductors for practical applications such as photocatalysts.

Scale of band gap energy influences the practical application of photocatalysts on the

redox ability and the energy required for exciting charge carriers. For wide band gap as example, large scale of band gap provides wide scale of redox potential on more species of target compounds; on the other hand, the acquired energy for exciting charge carriers is higher. The band gap scale is directly influenced by the particle size especially when the particle size is under nano-scale and the quantum effect occurred.[16]

For particles with size about tens of nanometer have extended band gap scale compared with those having larger size. As a consequence, higher energy light source is needed for quantum-sized semiconductors. Even so, larger band hap scale shows wider redox potential and is more available in degradation of pollutant.[16]

TOPO has been investigated for synthesis of nano-crystals. For nano-size materials, the 3D structure affects some physicochemical properties especially for optical and electrical device. The emission and absorption energies of the nanoparticles can be adjusted with the particle sizes, and the polarization of the emission can be controlled with the particle shape. To control the particle size and shape, the synthesis of nanoparticles usually involves the using of terminating and/or stabilizing agents. One of the approaches to terminate and to stabilize quantum-sized nanoparticles is capping the particles by amphoteric surfactant, TOPO. This agent has been mostly use to synthesize light emission quantum dots, like CdS, CdSe and CdTe. Those semiconductors provide a controllable approach for emission wavelength. For such kinds of materials, particle size makes a linear effect.[42,43]

Semiconductor photocatalysts also exhibit effective degradation of inorganic and organic pollutants in air and water. Above all of the semiconductors, TiO_2 presents a widely and practical application for environmental purification. Though commercial P25 has high degradation rate for many pollutants, its band gap range is 3.0-3.2 eV. Quantum crystal TiO_2 with intrinsically wider range of band gap can be applied for particular redox reactions. Complex pollutants such as endocrine disrupting chemicals (EDCs) are not effectively minimized by photocatalytic reaction. Some reaction byproducts are more toxic than original

17

one. TiO$_2$ with band gap energy higher than 3.2 eV is quantum affected, and has potential for specific environmental application. Additionally, nano-particles with high surface to volume ratio can provide more surface actives sites either on adsorption or reaction. Trentler et al.[13] and Joo et al.[14] have successfully synthesized nano-crystal of TiO$_2$ and ZrO$_2$, respectively. Using TOPO as stabilizing agent effectively prevents condensation and inhibits the growth of crystals at high temperature condition. TOPO a stabilizer chelates to the metal ions during preparation. Along with the formation of oxo bonds, TOPO terminates the condensation by chelating to metal ions which gives rise to small size particles. Because of the highly thermal stability of TOPO, it is suitable for high temperature environment without corrosion or disruption. Based on this property, crystallization can occur during preparation process at high temperature.   As a result, the final products exhibit homogeneous particle size and highly crystalline structure according to the HRTEM images.

Table 2-3.   Modifiers and their functions for phtocatalysis.

Method	Materials	Functions	Target compound	Ref
Sol-Gel	Trifluoroacetic Acid	Electron trapping	Acetone	[2]
	Activated carbon	Absorption	Dichloromethane	[38]
	Phosphate	Stabilizer, acidity	*n*-pentane	[2]
	MCM-41	Acidity enhancement	Phenol	[44]
Chemisorption	Vitamin C / Ascorbic acid	Sensitizer for solar light	Methyl orrange	[25,41]
Reduction precipitation with H$_2$	Pt	Electron trapping	Phenol	[22]
Combination of microemulsion and solvothermal	CdS	Sensitizer for solar light	Methylene blue Nitric oxide	[20]
Ion-exchange and impregnation	Zeolite	Acidity enhancement	NO	[45]

2-2-4 Modification with phosphorous groups

Several literatures have proved that treatment with acid process can enhance the thermal stability and photocatalytic activity of photocatalysts. Surface acidity of catalysts affects much on the selectivity and efficiency of phtocatalytic reaction. Surface Bronsted acid sites are always considered to be involved in the formation of hydroxyl radicals. Unsaturated Ti ions as Lewis acid sites adsorb oxygen and water molecules for further charge tapping. Hydroxyls groups of surface acid species such as nitric, sulfuric and phosphoric acids are common taken for enhancing the surface acidy of TiO_2. Colon et al. have used nitric, sulfuric and phosphoric acids for pre-treatment. The phosphoric acid treated TiO_2 exhibited higher thermal stability and excess adsorbed proton than untreated ones.[46] Nevertheless, the degradation of phenol was not as good as untreated TiO_2 did. Stone et al. also reported that phosphorous groups from surfactant (dodecyl phosphate) remaining on TiO_2 suppressed the quantum yield of transformation of acetone from 2-propanol.[8] Phosphorous species on TiO_2 seem to poison the active sites or act as sites for recombination of charges.

The number of phosphorous on TiO_2 significantly affects the photocatalytic activity. In the research published by Korosi[10], it was presented that higher content of phosphorous (P/Ti = 0.1) improved the thermal stability of TiO_2 but shown lower activity on degradation of phenol compounds. Higher content of phosphate were incorporated on surface layer as core-shell structure that the surface of TiO_2 was covered by phosphorous groups. Thus, higher content of phosphorous on surface (P/Ti = 0.05 and 0.1) cause the modified TiO_2 to have lower photocatalytic activity by inhibiting the surface degradation reaction. Phosphorous groups within TiO_2 can effectively retard the crystalline structure transformation by the increase of content of phosphate. Amorphous and semi-crystalline structure both behaves lower activity than crystalline TiO_2 with anatase form. Low crystallinity reveals more defects on surface or in the bulk and these sites are usually involved in recombination of electron and hole. That is the possible reason why high content of phosphorous can

reduce the photocatalytic activity of TiO_2. This is similar to the properties of mesoporous molecular sieves of titanium oxide synthesized by Stone et al. which had atomic ratio P/Ti = 0.68 and low activity. However, the optimal P/Ti molar ratio 0.01 successfully enhanced the photocatalytic activity from Korosi's observation. In other research, Yu et at. prepared a high actively phosphated mesoporous TiO_2 via 0.003 mole of H_3PO_4 and 0.03 mole of TTIP showing better activity than untreated mesoporous TiO_2 after calcined at 600 °C. Thus, it was suggested that higher phosphorous atoms on surface of TiO_2 inhibits the active reaction by the cover of phosphate groups on the surface active sites of TiO_2.

Because of low P/Ti ratio, some physicochemical properties of phosphated TiO_2 provides advantages for photoactivity. Crystallinity of phosphated TiO_2 was influenced by amount of phosphorous introduced which would retard the transformation temperature. TiO_2 with anatase phase exhibits better activity than amorphous or semi-crystalline TiO_2 which have more defects in bulk phase. Both appropriate calcinations condition and amount of phosphorous are needed to be emphasized. The treatment order with phosphorous groups seems not be the dominate parameter. Either introducing phosphoric acid into sol solution or immersing the gel or solid crystal in phosphate solution inhibit the collapse of porous structure, retard phase transformation and enhance the photoactivity.[9,2,10]

The surface-phosphated TiO_2 was also proved to have some properties such as higher acidity and specific surface area. Chemical bonding of phosphorous atoms on TiO_2 with excess OH groups are suggested as surface Bronsted acid sites for hydroxyl radical formation. Tetrahedral coordinated Ti ions with phosphorous atoms (Ti-O-P) are the other surface acid site, Lweis acid sites. Yu at al. distinguished octahedral and tetrahedral coordinated Ti from XPS spectra and Bhaumik et al. observed form XANES.[2,47] Both results indicated that tetrahedral Ti can adsorb more OH groups which was proved by measurement of surface isoelectric point and anion exchange capacity. Other researchs also claimed that the surface of phosphated TiO_2 have higher OH groups measured by NH_3 adsorption-desorption behavior

via TPD[9,48].   With phosphate groups on surface, TiO_2 would somewhat be negative charged in neutral aqueous solution.   Some positive charged pollutants would be attracted on phosphated TiO_2 and concentrated before oxidized during irradiation.   Zhao et al.[49] and Vohar et al.[50] have used negative-charged TiO_2 to degrade positive-charged compounds. Highly efficient adsorption and photocatalytic oxidaiton was observed.
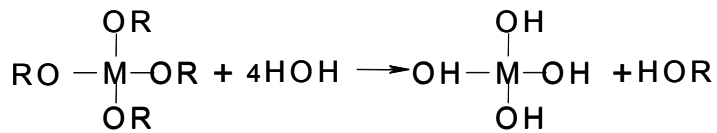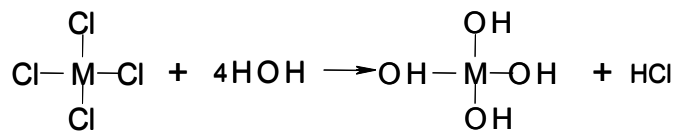
In order to fabricate high surface area materials, surfactant assisted method has been investigate for preparation of porous structure.   Interaction between head groups and alkyl metal precursors really affect the properties of metal oxide products. Some anionic surfactants have been used for synthesis of mesoporous structure such as dodecyl phosphate, and SDS.   Though through solvent extraction and calcination can remove most parts of the surfactant, phosphorous and sulfuric groups still remain in structure.   Stone et al.[8] and Wong et al.[51] have synthesized highly thermal stable and surface area mesoporous titanium and zirconium oxide.   However, the titanium mesoporous material has no effective transformation of acetone from 2-propanol and both materials have high content of phosphorous according to chemical analysis.   The content of phosphorous plays a critical role on photocatalytic reaction.

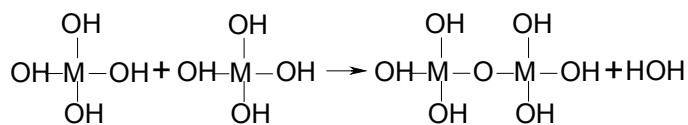## 2-3   Sol-gel method toward metal oxide

2-3-1   Hydrolytically sol-gel process

Sol-gel method has been used to prepare glass and other ceramic materials.   This is a versatile, easily performing in laboratory, and low cost method.   Three processes included for formation from colloidal sol solution to gel phase are hydrolysis of precursors, condensation between hydroxyl groups and finally gelation to gel phase. Precursors are usually metal halide and metal alkoxide.[52]   As Figure 2-10 shows, sol-gel method is very versatile for making films and powders for coating or other fabrication.   Dip coating and spin coating are mostly used for prepare films with sol-gel process.
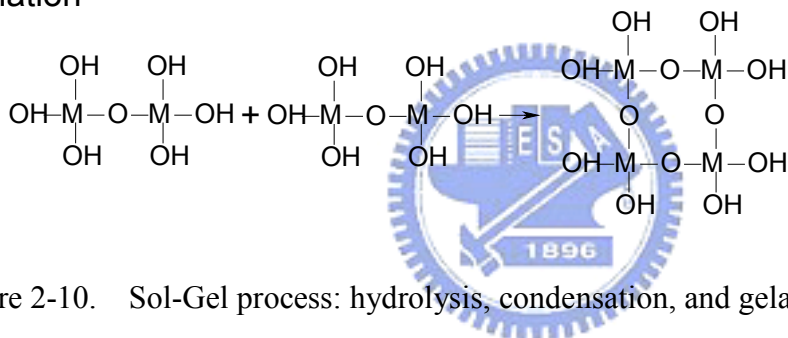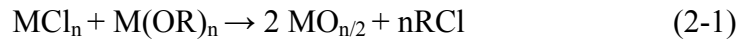
Hydrolysis

$$\mathrm{Cl-\underset{\underset{Cl}{|}}{\overset{\overset{Cl}{|}}{M}}-Cl \ + \ 4HOH \longrightarrow OH-\underset{\underset{OH}{|}}{\overset{\overset{OH}{|}}{M}}-OH \ + \ HCl}$$

$$\mathrm{RO-\underset{\underset{OR}{|}}{\overset{\overset{OR}{|}}{M}}-OR \ + \ 4HOH \longrightarrow OH-\underset{\underset{OH}{|}}{\overset{\overset{OH}{|}}{M}}-OH \ + HOR}$$

Condensation

$$\mathrm{OH-\underset{\underset{OH}{|}}{\overset{\overset{OH}{|}}{M}}-OH + OH-\underset{\underset{OH}{|}}{\overset{\overset{OH}{|}}{M}}-OH \longrightarrow OH-\underset{\underset{OH}{|}}{\overset{\overset{OH}{|}}{M}}-O-\underset{\underset{OH}{|}}{\overset{\overset{OH}{|}}{M}}-OH + HOH}$$

Gelation

$$\mathrm{OH-\underset{\underset{OH}{|}}{\overset{\overset{OH}{|}}{M}}-O-\underset{\underset{OH}{|}}{\overset{\overset{OH}{|}}{M}}-OH + OH-\underset{\underset{OH}{|}}{\overset{\overset{OH}{|}}{M}}-O-\underset{\underset{OH}{|}}{\overset{\overset{OH}{|}}{M}}-OH \longrightarrow \ldots}$$

Figure 2-10. Sol-Gel process: hydrolysis, condensation, and gelation toward metal oxide.[52]

2-3-2 Non-hydrolytically sol-gel process

However, sol-gel process occurs in hydrolytic solution is too fast to control even at room temperature. In order to fabricate homogenous and ordered arrangement, less reactive precursors, chemical modification of the precursors or other alterative method are used. Non-hydrolytic sol-gel method is also included. Unlike conventional hydrolytic sol-gel method, no hydrolysis is involved in non-hydrolytic sol-gel process. The major reactions involve the condensation between metal chlorides and metal alkoxides, or the formation of alkoxide functional groups in situ between metal chlorides and ether (or alcohol). As presented by equation 1 to equation 4. These condensation reactions do not occur at room

temperature. Usually heating up to 80 to 150 °C is needed for condensation. The main reaction between metal alkoxides and metal chlorides at room temperature is redistribution between functional groups (eq 5.).
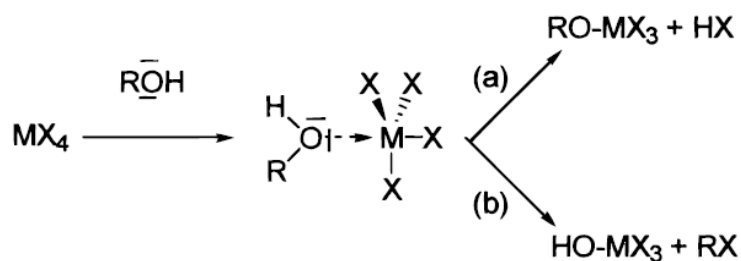
$$MCl_n + M(OR)_n \rightarrow 2\ MO_{n/2} + nRCl \qquad (2\text{-}1)$$

Condensation

$$\equiv MCl + R-O-R \rightarrow \equiv MOR + RCl \qquad (2\text{-}2)$$

$$\equiv MCl + H-O-R \rightarrow \equiv MOR + HCl \qquad (2\text{-}3)$$

$$MCl_n + n/2\ R-O-R \rightarrow MO_{n/2} + nRCl \qquad (2\text{-}4)$$

Etherolysis or Alcoholysis

$$\equiv M-Cl + \equiv M-OR \rightarrow \equiv M-OR + \equiv M-Cl \qquad (2\text{-}5)$$

Ligand Exchange

As for etherolysis and alcoholysis reaction initiate with lone pair electrons of oxygen attacking central metal, meanwhile hydrogen-halide and alky-halide bonding are forming (scheme 1.).

Scheme 1. Alcoholysis between metal chloride and alcohol.[11]

24

The condensation reaction begins with coordination of lone pair of electrons from an alkoxyl oxygen to metal center, followed by the cleavage of halide and alkyl groups and the bonding of alkyl halide (eq 6).

$$M-OR+M-X \rightleftharpoons \begin{matrix} M-X \\ | \\ M-O-R \end{matrix} \longrightarrow M-O-M+RX \qquad (2\text{-}6)$$
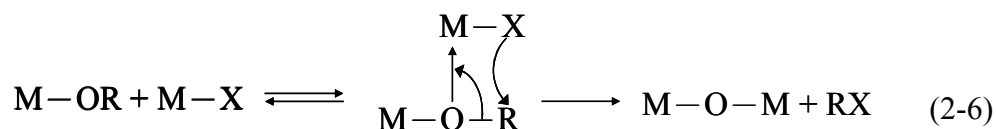
A. Vioux and co-workers have reported the synthesis of inorganic oxides by non-hydrolytic sol-gel method, like, silicon oxides, aluminum oxides, titanium oxides and zirconium oxides; moreover, binary oxides are also successfully prepared by this method.[11,53-55]

The reaction rate can be catalyzed by iron chloride and aluminum chloride which acts as Lewis acid. In addition to inorganic oxides, organic-inorganic hybrids materials are also capable via non-hydrolytic sol-gel method.[56] Therefore, by non-hydrolytic sol-gel method inorganic and organic-inorganic hybrids materials can be conveniently prepared.

2-4   Calcination effects

Solid products obtained by sol-gel method usually need further treatment with high temperature for rearrangement of atoms to crystalline structure. Crystalline TiO_2 has higher and wider applications. Calcination at high temperature changes some physicochemical properties of un-calcined samples. Therefore, calcination process is expected to bring both advantages and some drawbacks on different applications. Calcination under air atmosphere reasonably provides a highly oxidizing condition. The following statements are about calcination effects on surface properties, electronic properties and microstructure under air atmosphere.

2-4-1　Surface properties

For pure TiO_2, the surface usually bounded with hydroxyl groups (Bronsted acid site) due to the water molecules around in air.　Those hydroxyl groups are bounded with the unsaturated Ti^{4+} ions which are in tetrahedral coordination and the oxygen vacncy.　The more of surface hydroxyl groups, the more the induce hydroxyl radicals will be induced for higher reaction rate.　When temperature rises to certain degree, dehydroxylation occurs as a consequence the number of surface hydroxyl groups decreases.　Lower defect sites on the surface of TiO_2 result in lower hydroxyl radical will be induced.　Modification of certain compounds needs specific heating treatment for surely chemisorbed of this compound on the surface of TiO_2.　Jimmy C. increased the heating temperature to 250 °C for chemisorbed of trifluoroacetic acid on the surface of TiO_2 which owns higher photoactivity for degradation of acetone.[2]　Polystyrene used as template was calcined in the flow of air at 600 °C and turned to graphite deposited on the surface of TiO_2.[57]　Graphite presented on the surface of TiO_2 works for suppression of phase transformation.
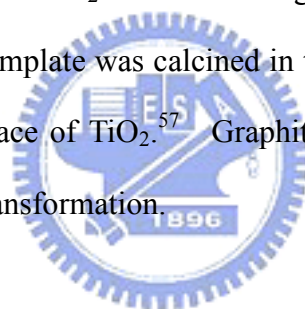
2-4-2　Microstructures

High temperature treatment provides energy for rearrangement of atoms.　Amorphous sol-gel products are always treated by heating for crystalline structure formation.　At about 300-400 °C, anatase TiO_2 will be emerging.　Anatase form is metastable ready to transform to more stable rutile form under high temperature treatment (around 500-600 °C).　The rearrangement of Ti and O atoms for rutile form structure results in lower defects in the bulk and on the surface.　The defect sites are somehow also active sites for trapping charge carriers and for reactions.　One of the reasons why rutile form presents lower photoactivity than anatase form is the less number of defects within rutile structure.　Providing energy from high temperature makes the crystals growth to larger size.　The crystalline range of crystals extends with the increase of temperature.　As a result, the band gap decreases from

quantum effected-scale to bulk-scale, 3.0 eV of TiO_2 as example, with shorter range of redox potential. Moreover, sintering occurs along with the crystal growth. The boundary is broken by the growth of crystals between two grains. Fusion of grains induces the final products with multi-crystalline and larger particle size. Larger size of particles show lower surface area and this is a disadvantage for application in photocatalysis and absorption. Multi-crystalline particles behave more defects inside bulk phase which are also the recombination sites of charges.

2-4-3 Electronic structure

Electronic structure measured from UV-visible absorbance is followed by the absorption edge in UV-vis spectrum. Heating provides energy for rearrangement of atoms results in more condensed and stable structure. Take TiO_2 as example, anatase form is less stable than rutile form, and the band gap of anatase and rutile are 3.2and 3.0 eV, respectively. Moreover, the quantum effect disappears when the particle size growth with the increase of heating energy. Nano-sized (tens nanometer) TiO_2 particles gave band gap energy higher than 3.2 eV which returns to 3.2 eV when particle size increases larger size beyond nano-scale.

Chapter 3.   Materials and Methods

Figure 3-1 shows the flow chart of the experimental arrangement in this study. Catalysts are synthesized with non-hydrolytic sol-gel process and the prepared samples are moved to be heated at 250, 350, 450, 550, 750, and 950 °C for 3 hours.   The calcined samples are characterized by several techniques, such as XPS, XRD, TEM, FTIR, UV-vis, and BET. As-prepared samples are first analyzed by TA/DSC.   Photocatalytic activities on bleaching of RhB of as-prepared and calcined samples are tested.   Relationship between calcinations effects and photobleaching on RhB will be investigated.

3-1   Materials

Titanium chloride ($TiCl_4$, Fluka, 99 %) and zirconium isopropoxide propanol complex ($Zr[OCH(CH_3)_2]_4 \cdot (CH_3)_2CHOH$, Aldrich, 99.9 %) were used as the precursors of titania and zirconia, respectively.   Trioctylphosphine Oxide (TOPO, $[CH_3(CH_2)_7]_3PO$, Fluka, > 98.0%) is used as stabilizer for controlling the particle size growth and solvent in the NHSG process. Because the $TiCl_4$, $Zr[OCH(CH_3)_2]_4 \cdot (CH_3)_2CHOH$, and TOPO are moisture sensitive, these chemicals are stored in a glove box.   Rohdamine B (RhB, $C_{28}H_{31}N_2O_3Cl$, Sigma Aldrich, Dye content 95%) was used as the target compound for photocatalysis and its structure is shown in Figure 3-2. H_3PO_4 (Merck, 85%) was used as the phosphorous source for the preparation of phosphated TiO_2 using conventional impregnation method. $NaClO_4$ (ACROS ORGANICS 99%) was used to stabilize the ionic strength and NaOH (J.T.Baker, 98.0%) and HCl were taken to adjust the pH value of solid suspension for measurements of surface zeta potential.
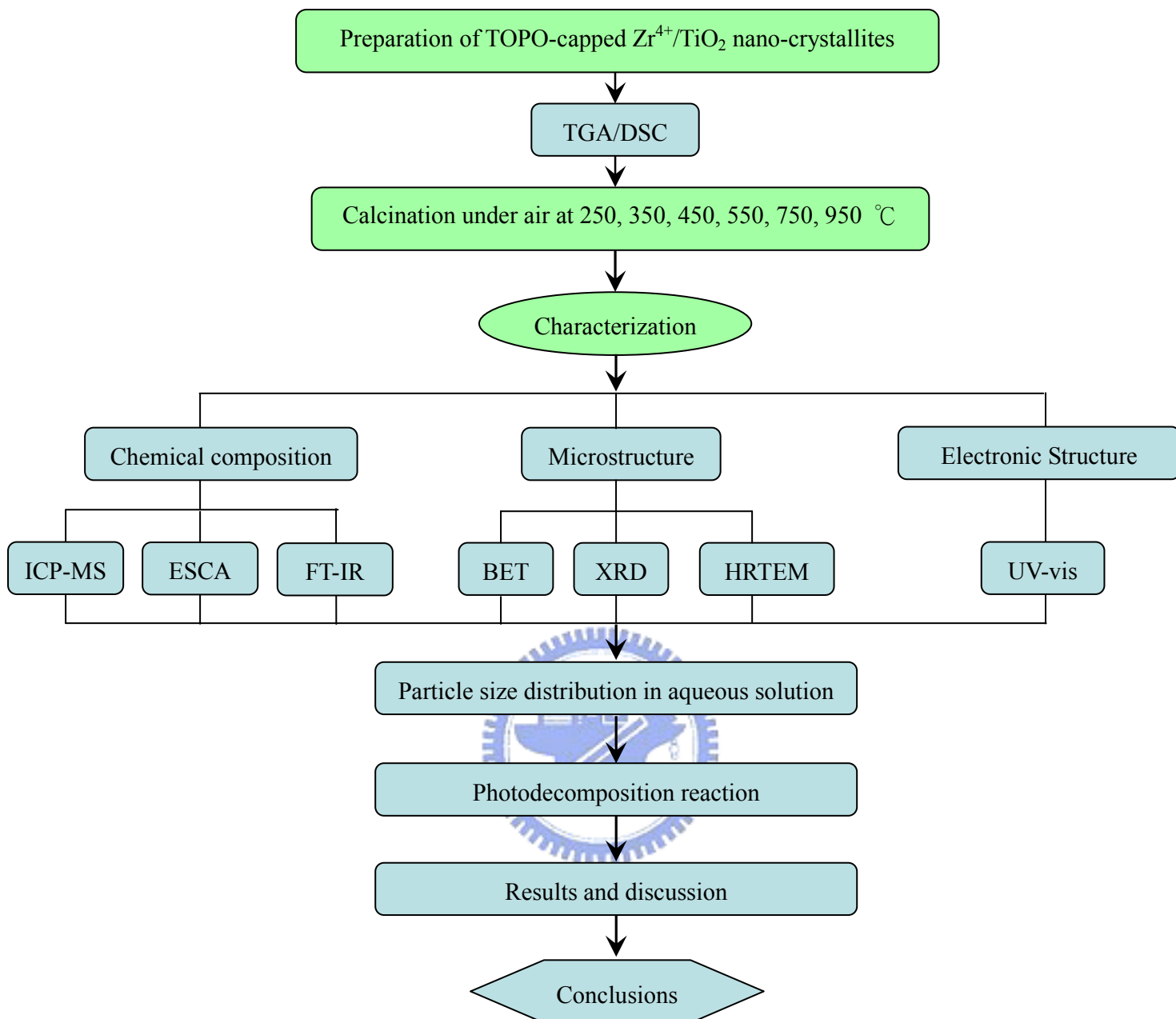
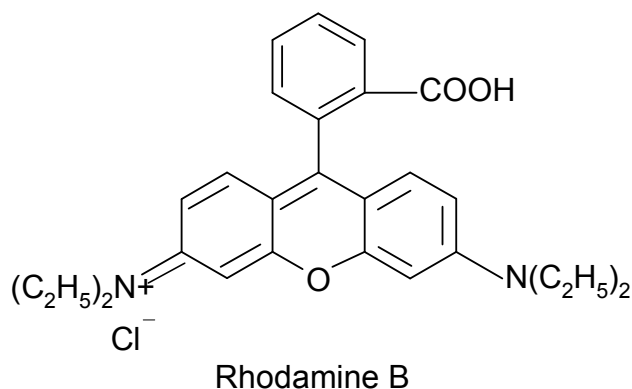Figure 3-1.   Flow chart of experimental design in this study.

Figure 3-2.   Structure of Rhodamine B

3-2   Preparation of TOPO-capped Zr^{4+}/TiO_2 via NHSG process

TOPO-capped Zr^{4+}/TiO_2 are prepared by a non-hydrolytic sol-gel process.   5.22 g of TOPO (13.5 mmole) and 0.75 g of zirconium isopropoxide propanol (1.0 mmole) were added in sample vials (12 mL, OD×H = 19×65 mm) and moved to hotplate.   The mixtures were heated at 80 °C with stirring at 500 rpm for melting TOPO and dissolving the precursors into the TOPO.   0.276 ml of $TiCl_4$ (2.5 mmole) was injected into the solution by 1.0 ml syringe followed by increasing the temperature to 150 °C and maintained this temperature for 15 minutes.   Afterwards, the temperature was increased to 400 °C for 3 hours with N_2 flow in a homemade glassware cap (Figure 3-3).   The solution turned gradually from transparent yellow to opaque grey during synthesis.   When the synthesis was completed, the solution was naturally cooled down to 60 °C.   Acetone was used to wash out residual TOPO and other organic by-products.   The products were separated from the solutions by centrifugation at 11000 rpm for 10 minutes.   This washing step was repeated for three times. The samples were dried under ambient condition for few hours and then grinded with agate mortar into fine powders.   The product is proved to be well dispersed in non-polar solvent such as acetone and hexane.
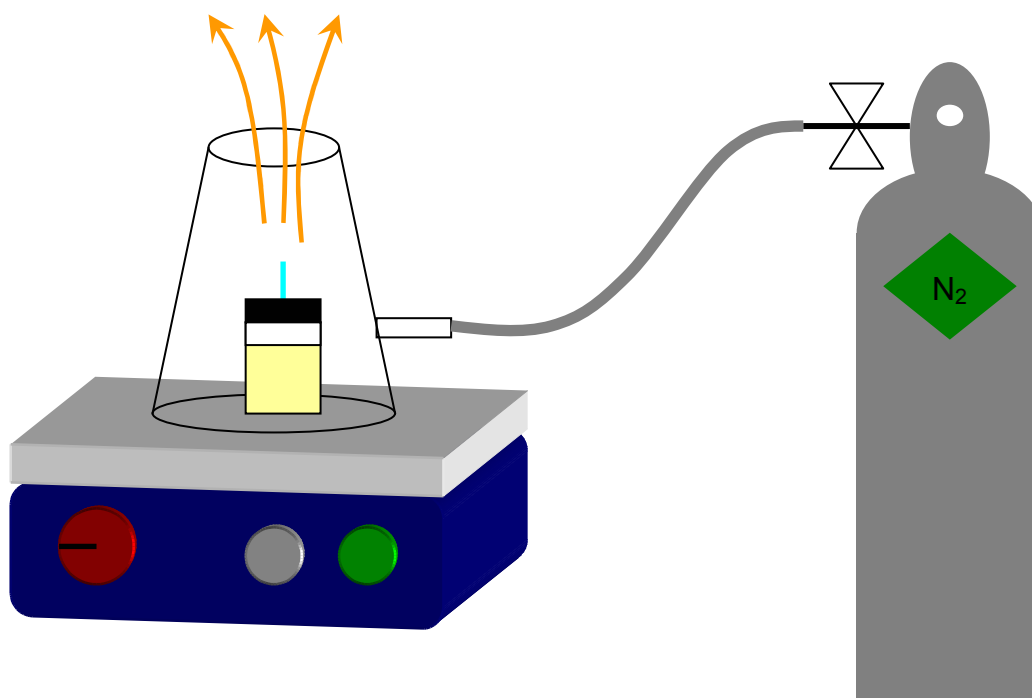
Figure 3-3.   The apparatus for synthesis of NHSG derived TOPO-capped Zr^{4+}/TiO_2.

3-3   Calcination

The NHSG-derived samples were calcined in a tube furnace (Lindberg/Blue M 1200 °C Tube Furnaces / Eurotherm 818P) at various temperatures (250 °C, 350 °C, 450 °C, 550 °C, 750 °C, and 950 °C) in air for 3 hours and naturally cooling to room temperature.   The temperature rose from room temperature (around 25 °C) to the target temperatures at 10 °C/min.   All the samples were carried in an aluminum oxide boat.

3-4   Conventional method for phosphated TiO_2

Conventional method for preparation of phosphated TiO_2 was to impregnate 0.5 g Degussa P25 powders with 50 ml phosphorous acid solutions that have different concentrations (0.1, 0.2, 0.3, 1.0, 3.0, and 5.0 M).   The impregnation was proceed under vigorous stirring for 5 hr.   The TiO_2 were collected by centrifugation at 1100 rpm for 10

mins and then removal of supernatants.   The samples were then dried at 200 °C for 3 hr and grinded to fine powders for further characterization and photocatalytic experiments.

3-5   Characterization

3-5-1   Thermogravimetric Analysis/Differential Scanning Calorimetry (TGA/DSC)

Thermogravimetric and differential scanning calorimetry (TA/DSC) is used to understand the mass loss and energy flow during heating treatment from room temperature to 1000 °C in air (Appendix A-1.).   The TA/DSC was performed under air flow of 50 ml/min and at heating rate of 10 °C/min from 25 to 1000 °C on Seiko SSC 5000.

3-5-2   Electron Spectroscopy for Chemical Analysis (ESCA)

The surface chemical compositions and chemical states of the NSGH-derived nanocrystalls before and after calcination were characterized by ESCA (ESCA PHI 1600) using an Al Kα X-ray source (1486.6 eV).   The photoelectrons were collected into the analyzer with a 23.5 eV pass energy (Appendix A-2.).   The collection step size in wide range scan and high-resolution analysis are 1.0 eV and 0.1 eV, respectively.   All analytical process was controlled under ultrahigh vacuum conditions at the pressure below 1.4×10^{-9} Torr.   The chemical shift in binding energy of XPS spectra was referenced to the O(1s) line as 530.2 eV.   Detailed operational parameters are listed in Appendix A-3.

For advanced qualification and quantification of each element, curve fitting of XPS spectra was performed on program.   After performing a Shirley type background subtraction, the original spectra were fitted using a nonlinear least-squares fitting program and Gaussian-Lorentzian peak shapes were adapted for all peaks.   The parameters used for the curve fitting of the Zr 3d, O 1s, P 2p, Ti 2p, and C 1s, including the binding energies, doublet

separation, and curve area.   The atomic ratios were calculated from the integrated peak areas normalized to sensitive factors.   The equation for atomic ratio calculation is shown below:

$$\frac{n_1}{n_2} = \frac{I_1 / ASF_1}{I_2 / ASF_2} = \frac{A_1 / ASF_1}{A_2 / ASF_2}$$

(3-1)

Where n denotes the atomic numbers, I is the intensity of species on XPS spectra, A is the peak area, ASF stands for the atomic sensitive factor of element and Arabic number represents elemental types.

3-5-3   Fourier-Transform Infrared Spectrometer (FT-IR)

The surface functional groups of the nanocrystals before and after calcinations were analyzed on Fourier-transform infrared spectrometer (FTIR, Horiba) scanning from 400 to 4000 cm^{-1} with a resolution of 4 cm^{-1} for 100 scans.   Powder samples were mixed with KBr (Merk) and pressed as a flake for the FTIR measurement (Appendix A-4.).

3-5-4   High resolution transmission electronic microscope (HRTEM)

The particle size and shape of nanocrystals were examined by a high resolution transmission electronic microscopy (HRTEM, JEOL JEM-3000F) at an accelerating voltage of 300 KV.   The specimen was prepared by dispersing of powders into acetone with ultrasonic vibration.   The colloidal was dropped on a holey carbon film supported on a Cu grid.   Low-magnification TEM images are displayed in Appendix B.

3-5-5　X-ray powder diffractometry (XRPD)

The crystalline structure of the nanocrystals were identified via X-ray powder diffractometry (XRPD, MAC Sience, MXP18) using Cu Kα irradiation (λ = 0.1546 nm) and operating at accelerating voltage of 30 KV and an emission current of 20 mA.　The X-ray patterns were acquired from 20° to 90° 2θ at a sampling width of 0.02° and a scanning speed of 4 °/min (Appendix A-5.).　Crystalline size (D) of each sample was estimated via Scherrer's equation:

$$D = \frac{0.89 \times 0.15406}{\beta \times \cos\theta} \tag{3-2}$$

Where β is the full width at half-maximum (fwhm).

3-5-6　UV/vis spectrometry

The optical properties of the nanocrystals were analyzed in terms of diffused reflectance spectrum using UV-vis spectroscopy (HITACHI 3010) scanning from 800 to 200 nm.　All the samples were reference to aluminum oxide which was considered to exhibit total reflections (Appendix A-6.).

The diffused reflectance F(R) was conversed to absorption type using Kubelka-Munk fomula[58]:

$$F(R) = \frac{(1-R)^2}{2R} = \frac{k}{S} \tag{3-3}$$

Where k is absorption coefficient, S is scattering coefficient and R represents %R reflectance.

3-5-7 Inductively Coupled Plasma Mass Spectrometry (ICP-MS)

ICP-MS (Perkin Elmer, SCIEX ELAN 5000) was used to analyze bulk chemical compositions including Zr/Ti and P/Ti ratios of samples.   All solid samples were digested with acid solution coupled with microwave.

3-5-8 Dynamic Light Scattering (DLS) and Zeta potential

The hydrodynamic diameter and surface zeta potential measurements were carried out by Zetasizer Nano ZS.

The zeta potential and particle size measurements are employable for particle size from 5 nm to 10 μm and 0.6 nm to 6 μm, respectively.

For hydrodynamic diameter measurement, the solid suspension was a 0.25 mM RhB aqueous solution containing catalysts of concentration of 1 mg/mL and was mixed well by ultrasonic for at least one hour.   The mixture was characterized with single angle 173° backscattering system incorporating a 633 nm laser as light source.

For zeta potential measurement, the suspension was a 0.1 M aqueous solution of $NaClO_4$. The concentration of catalysts in this solution was 0.4 mg/mL.   The pH value of suspension was adjusted by NaOH and HCl solution.

3-5-9 Specific Surface Area

The specific surface area, S_{BET}, was determined by BET multipoint technique on Micromeritics sorptometer (ASAP 2020) taking N_2 as the adsorbent.   Before analysis, all samples were pre-dried at 80-90 °C for 30 mins.   For providing sufficient surface area for model calculation, over 0.3 g of powders was used for analysis. Because surface TOPO molecules are sensitive to temperature, ass-prepared sample was degassed at 120 °C for 360

mins, and other samples were all treated at 150 °C for 240 mins.

3-6 Photocatalytic of RhB decomposition

Rhodamine B (RhB) was selected as target compound to test the photocatalytic activity of the nano-crystals before and after calcination.   The catalysts (15.0 mg) were dispersed ultrasonically into 15.0 ml of RhB solutions with concentration of 0.25 mM at least for 1 hr. The previous mixture was contained in a fused-silica tube with capacity of 17 ml.   Prior to irradiation, the suspension was purged with O_2 for 30 minutes for equilibrium of adsorption and desorption of RhB as well as saturation of the solution with O_2.   The purging was continued during photocatalysis.   The photocatalysis was carried out under illumination of UV light at 305 nm in the reactor (Figure 3-4).   The degradation of RhB was measured by their absorbance at 553 nm using UV-vis spectroscopy.   Quantitation of RhB was based on its calibration curve ranging from 0 to 0.05 mM (Appendix A-7.).

Figure 3-4.   Photocatalytic reactor with 6 UV light tubes of 305 nm set around the fused-silica tubes.

Chapter 4.   Results and Discussion

4-1   Thermal analysis

In order to understand the thermal behaviors during calcination under air atmosphere, TOPO-capped Zr^{4+}/TiO_2 nanocrystals were analyzed by thermogravimetric analysis and differential scanning calorimetry (TGA/DSC). Figure 4-1 displays the heat flow and weight loss from 25 °C to 950 °C. The curve can be divided into four parts: 25-100 °C, 100-300 °C, 300-500 °C, and 500-950 °C.

Between 25 and 100 °C, about 2% weight loss is denoted to the removal of surface physisorbed water molecules. From 100 to 300 °C, 2% weight loss is observed. In addition, exothermic process occurred at 250 °C.   This phenomenon suggests that the carbon are removed from TOPO and partially oxidized.   Actually the white as-prepared powders change into brown after calcined at 250 °C.

Between 300 and 500 °C, a significant weight loss (7%) accompanied with one exothermal peak centered at around 360 °C is observed indicating the oxidation of the organic compounds.   The organic species are completely burned out above 500 °C. Meanwhile, hydrophilic surface is readily to be obtained.   Since the as-prepared sample capped with TOPO has a hydrophobic surface and can be well dispersed in acetone or hexane, the TGA results indicate that the hydrophobicity of TOPO-capped Zr^{4+}/TiO_2 can be turned by calcination.

About 1% weight loss as temperature rose from 550 to 900 °C implies the removal of surface hydroxyl groups via dehydroxylation and deoxygenation.
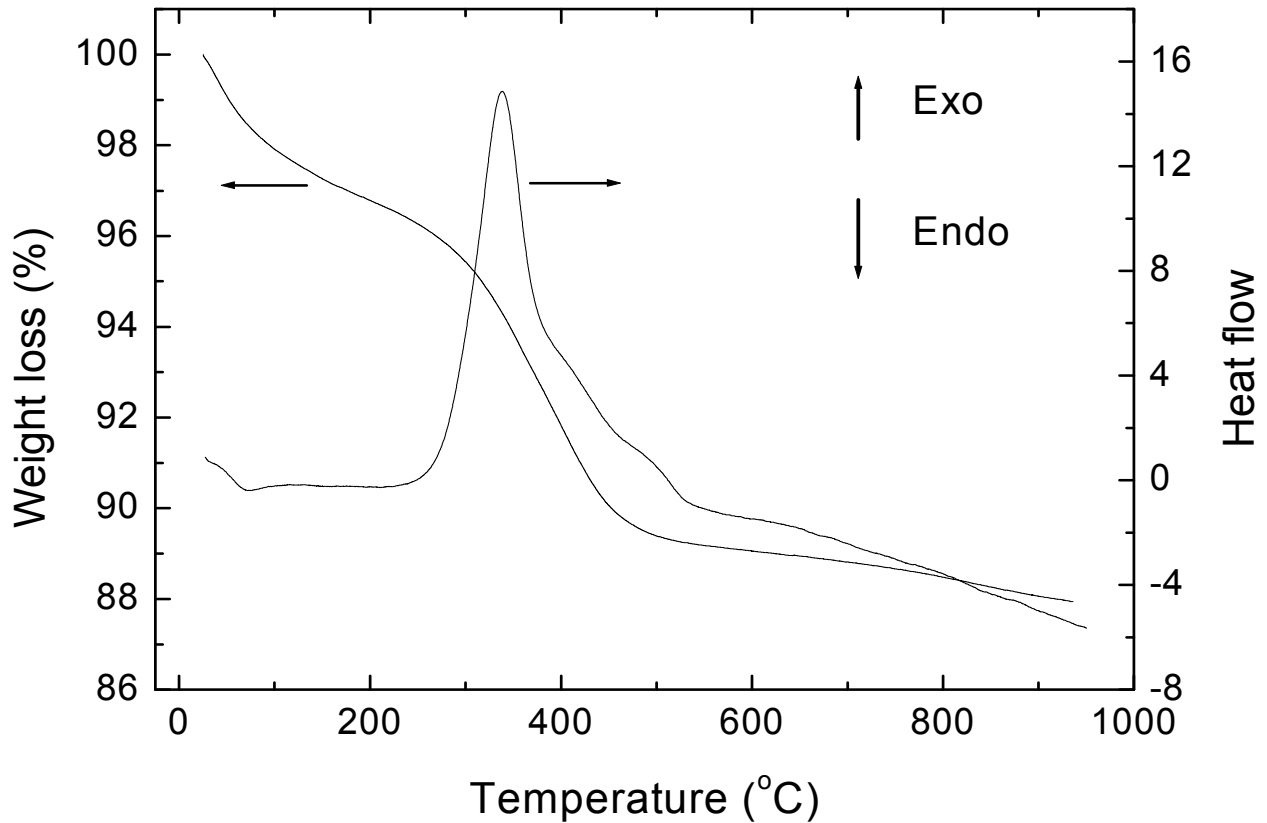
Figure 4-1. The TGA/DSC curves of the TOPO-capped Zr^{4+}/TiO_2 nanocrystals calcined in air.

4-2   Chemical composition

To understand the surface chemical properties before and after calcination, we use XPS to deduce the change of surface chemical compositions.   Figure 4-2 shows the wide range scanned XPS spectra of the TOPO-capped Zr^{4+}/TiO_2 before and after calcinations at various temperatures.   The Ti, O, Zr, and C elements are observed in wide scanning XPS spectroscopy indicating that the material is mainly composed of TiO_2, ZrO_2 and some carbonaceous compounds.   In additionally, phosphorous group (P2p) is also examined in high resolution scanning XPS spectroscopy (See Figure 4-3).   It is suggested that the phosphorous and part of carbonaceous groups are from the surface TOPO molecules on as-prepared nano-crystals.
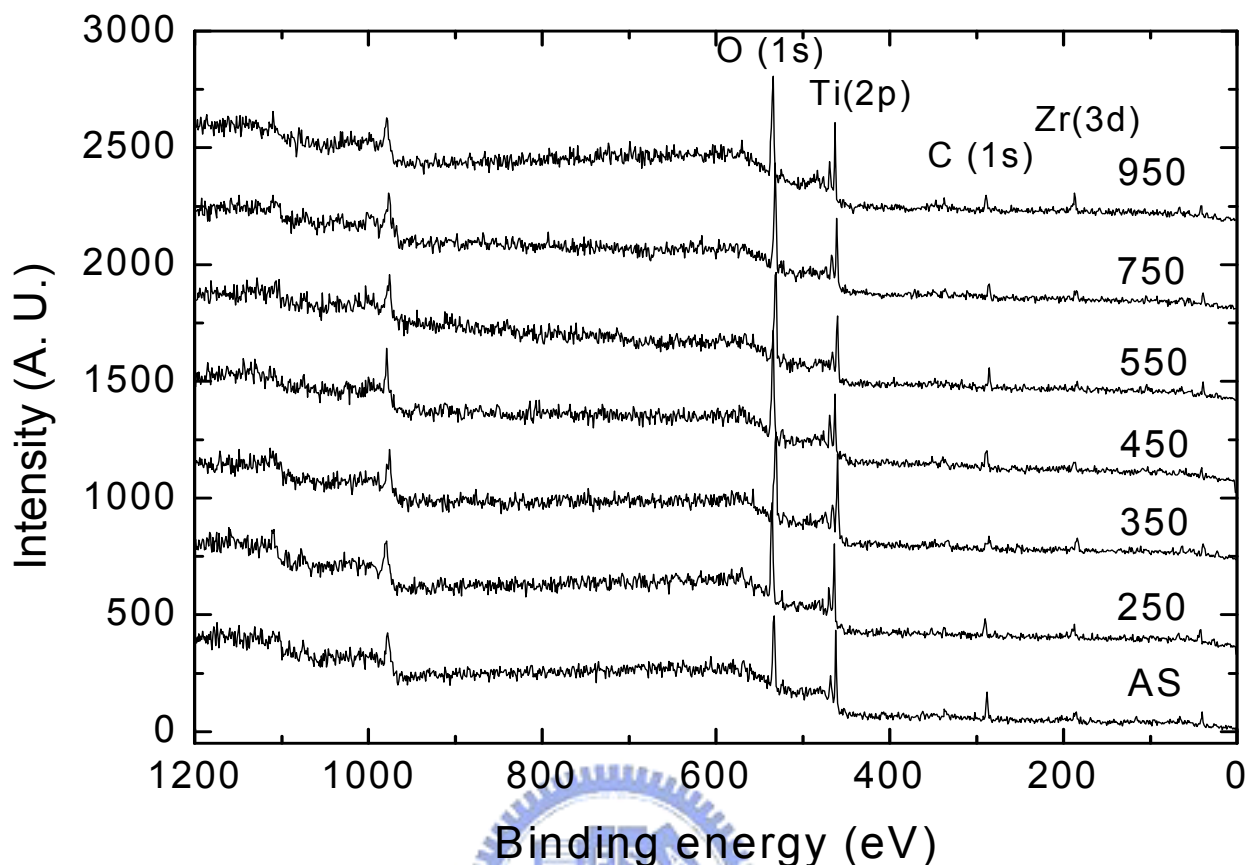
Figure 4-2. The wide-range scanned XPS spectra of the TOPO-capped Zr^{4+}/TiO_2 before and after calcinations at various temperatures.

For detail information, the high resolution scanning XPS spectra of P(2p) and C(1s) were also examined in Figure 4-3 and 4-4, respectively. The P(2p) binding energy of pure TOP, as-prepared and calcined samples were scanned form 125 to 145 eV. Pure TOPO has P(2p) binding energy of 131.8 eV from the P=O groups within itself. Peak of 132.7 eV is observed from as-prepared nano-crystals indicating that the phosphorous groups were oxidized to higher binding energy during non-hydrolytic sol-gel process. It is suggested that the phosphorous head groups of TOPO molecules involved in the condensation oxo bonding during preparation process. Compared to as-prepared sample, the calcined samples exhibit higher binding energy of 133.7-134.5 eV responding to the P^{5+} species of phosphate groups.

Because of the introduce of oxygen molecules into surface structure, surface groups are oxidized to higher oxidizing state during calcinations under air atmosphere. Moreover, dehyroxylation from phosphate groups leads the shift of P(2p) to lower binding energy above 500 °C.

Calcination in air atmosphere provides an oxidizing condition and effectively oxidized the surface phosphorous groups to higher oxidizing state of P^{5+} corresponding to phosphate salt. Thus, the TOPO-capped Zr^{4+}/TiO_2 nano-crystals are phosphated after heating process.

Figure 4-4 shows C(1s) high resolution scanning XPS spectra of TOPO-capped Zr^{4+}/TiO_2 before and after calcined at various temperature. As-prepared sample reveals two kinds of carbon species which are mainly from TOPO molecules of alkyl and C-P groups with binding energy of 284.6 and 283 eV, respectively. At 250 °C, the P-C groups of TOPO transform into another species with binding energy of 288.5eV corresponding to higher oxidizing state. Several studies have depicted that the binding energy increases with the increase of the number of oxygen molecules incorporated. Therefore, it is suggested that the carbon species with binding energy of 288.5 eV are C=O or O-C=O groups.[59] These partially oxidized carbon species are mainly the source of brown color observed after calcination at 250 °C.

From P (2p) and C (1s) high resolution scanning XPS spectra, it is suggested that the TOPO have involved in the condensation reaction during non-hydrolytic sol-gel process and retained on the surface of Zr^{4+}/TiO_2.

Surface functional groups have significantly influence on the photoactivity and reaction mechanism of photocatalysts. Especially, surface acidity has been investigated involved in the selectivity and efficiency of catalytic reactions.[60] Either Lewis or Bronsted acid sites are proved to enhance the photocoatalytic activity by increasing the surface hydroxide ions amount for the formation of hydroxide radicals. Surface phosphate modification also demonstrated to increase surface OH groups and inhibit the collapse of porous structure after

heating process.   The TOPO-capped Zr^{4+}/TiO_2 are also modified with phosphate groups after calcined in air atmosphere.   The phosphated nano-crystals are expected to exhibit higher photocatalytic activity.   In addition to phosphate groups, the partially oxidized carbonaceous groups are also ready to influence the photocatalytic reactions.
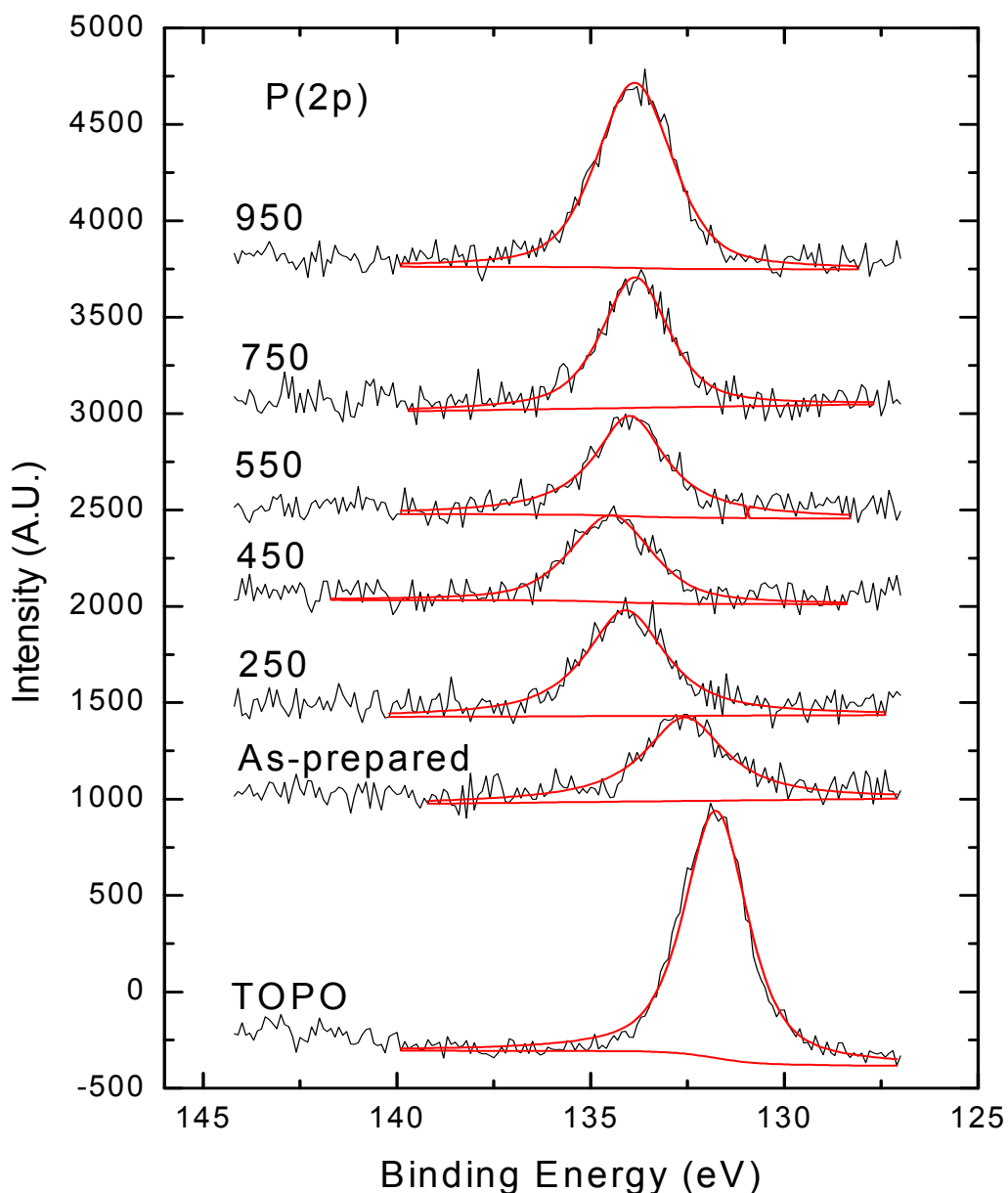

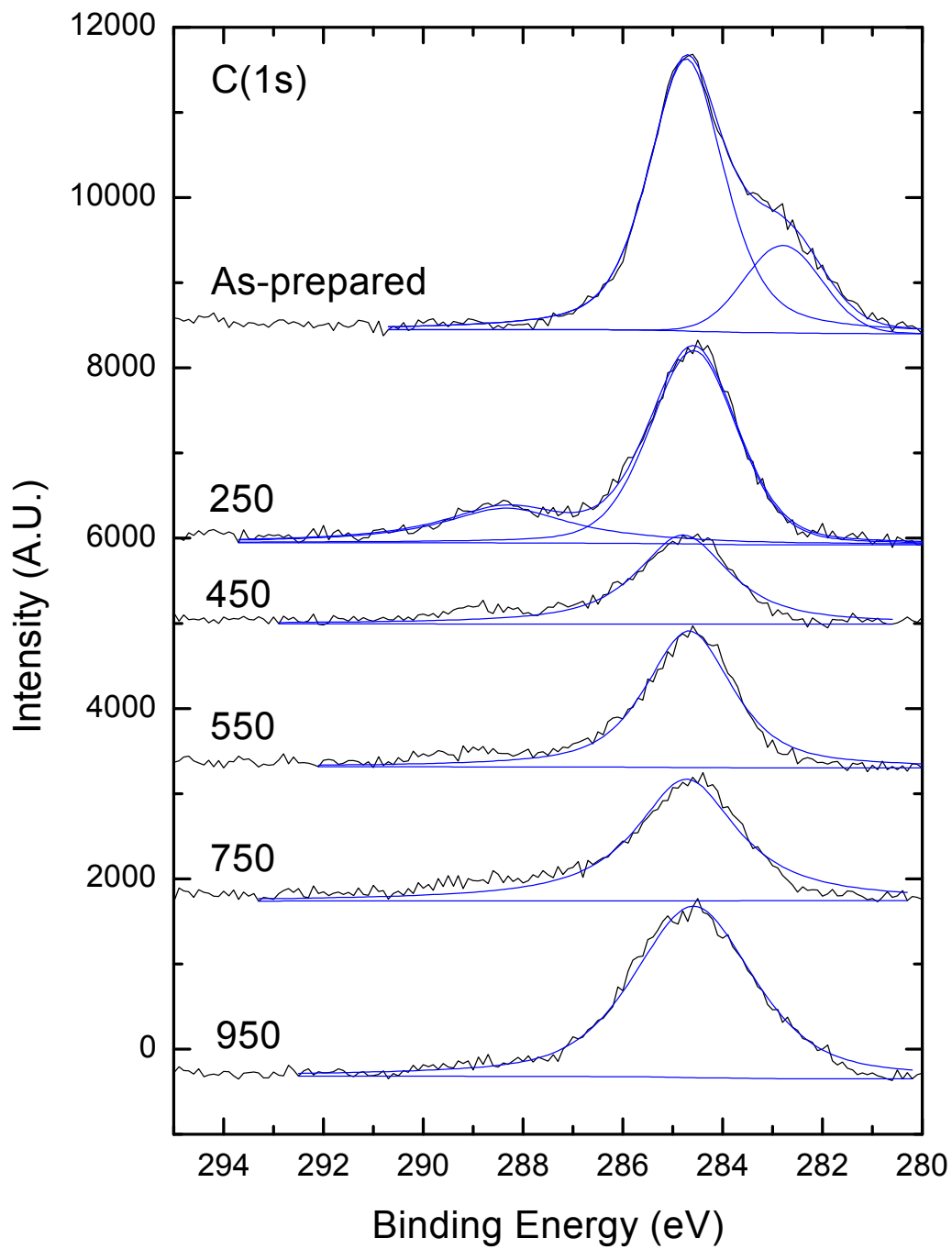Figure 4-3.   The evolution of P (2p) XPS spectra of the TOPO-capped Zr^{4+}/TiO_2 before and after calcination at elevated temperatures.

Figure 4-4. The evolution of C (1s) XPS spectra of the TOPO-capped Zr^{4+}/TiO_2 before and after calcination at elevated temperatures

To examine surface chemical properties, FT-IR is used to determine the surface functional groups of as-prepared and clacined samples. Figure 4-5 illustrates the FT-IR absorbance spectroscopy from 400 to 4000 cm^{-1} of TOPO-capped Zr^{4+}/TiO_2 nano-crystallites before and after calcined at different temperature.

The absorbance peaks at 2852 and 1460 cm^{-1} are surface alkane and -CH groups, respectively, observed both on pure TOPO and as-prepared sample. The sources of alkane groups on as-prepared sample are mainly from the surface capping TOPO molecules. At 250 °C, the intensity of surface carbon groups decreases accompanied with the increase in peak intensity at 3400 and 1650 cm^{-1} which correspond to physisorbed water and hydroxyl groups, respectively. The decrease in carbon groups is in good agreement with the result of TGA that the organic parts of TOPO are decomposed at elevated temperature. No absorbance of surface carbon species is observed at even higher temperature which is in agreement with TGA that the carbon groups are completely thermal decomposed during calcination. In contrast, the intensity of surface physisorbed water increases above 250 °C and keeps uniform till calcined at 950°C. Because of the decomposition of TOPO molecules by calcination, the surface of calcined samples were oxidized to more hydrophilic which can attract more water molecules on surface. However, higher calcination temperature at 950 °C has removed some surface OH groups as observed from weight loss of TGA curve and the decrease of absorbance at 3400 cm^{-1}. The broad absorbance around 850 cm^{-1} corresponds to Ti-O-Ti bondings.[2]

The absorption region at 900-1260 cm^{-1} is usually referring to stretch of phosphate groups including P=O and P-O bonds. Pure TOPO molecules have phosphorous groups of P=O with vibration frequency at 1150 cm^{-1}. Compared with TOPO molecules, as-prepared sample has phosphorous groups with lower vibration frequency at 1093 cm^{-1}, indicating that the phosphorous head groups chelate to titanium ions during non-hydrolytic sol-gel process. The chelating between phosphorous head groups and titanium ions is suggested to be

$P=O \rightarrow Ti$.[15,47]
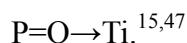
At high temperature of 250-750 °C, the calcined samples have similar surface phosphorous groups with broad vibration range of 1150-1019 cm^{-1}. Some phosphorous species correspond to higher oxidizing state with lower vibration frequency at 1019 cm^{-1}. This shift can correspond to the formation of O-P-O or PO_4^{3-} groups after heating in air. Moreover, no absorbance of P-O-P groups at 750 cm^{-1} is observed on as-prepared and calcined samples. The shift of phosphorous species to the region of 1105-1019 cm^{-1} on calcined samples is suggested to be the formation of P-O-Ti bonding to the surface layer after oxidized by heating in air.[2] Thus, after calcined at 250 °C, the sirface phosphorous groups are approved to be both oxidized and chemically bonded to surface metal ions in air atmosphere.

After calcined at 950 °C, the vibration intensity of P=O at 1105 cm^{-1} apparently increases. Because of surface dehydroxylation at 950 °C, some OH groups were removed from P-OH which contributes to the change of phosphorous species to P=O with lower vibration frequency.

During calcination process, surface capped TOPO molecules are thermal decomposed and the surface of calcined samples turn to hydrophilic with more hydroxyl groups on surface. The thermal decomposition of TOPO molecules also leads to the surface modification with phosphorous groups.
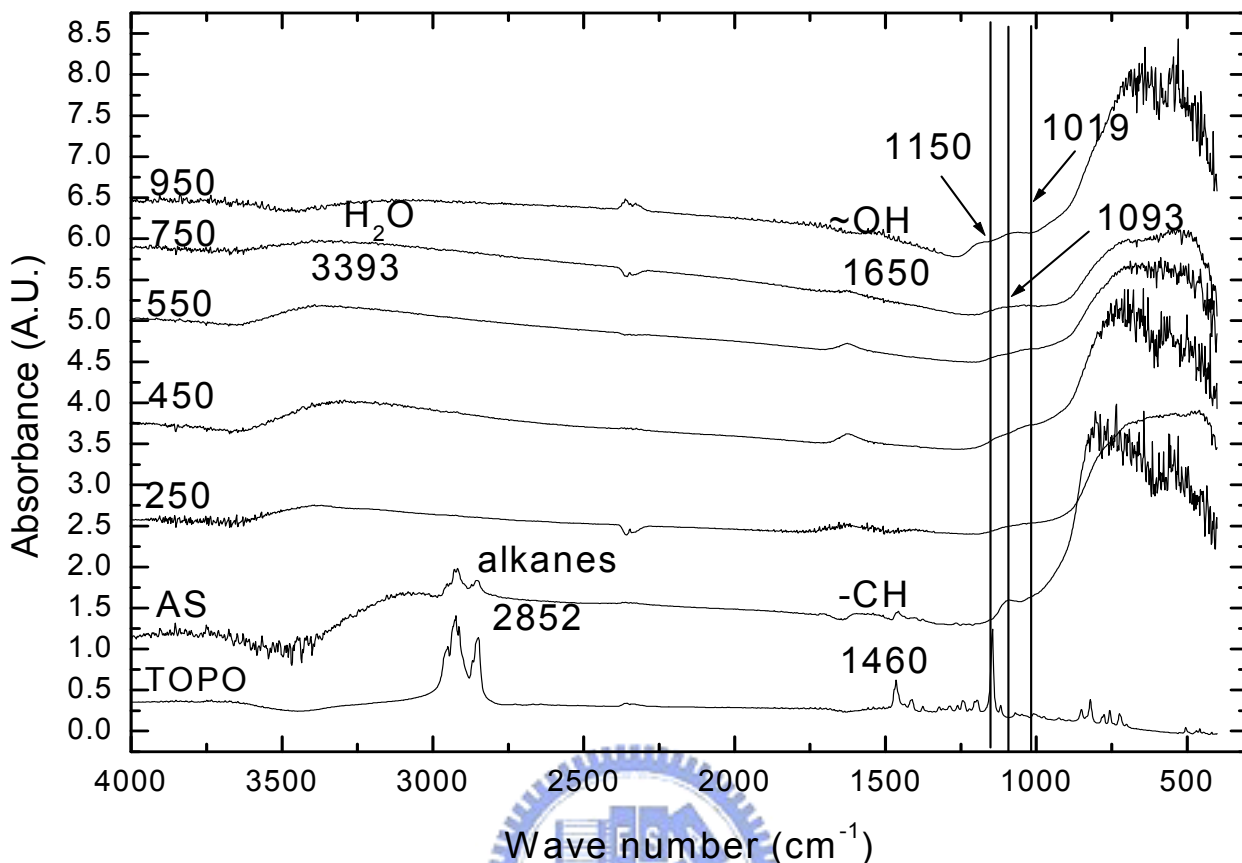
Figure 4-5. The FTIR spectra of the TOPO-capped Zr^{4+}/TiO_2 before and after calcination at different temperatures

To examine the chemical compositions of TOPO-capped Zr^{4+}/TiO_2 nano-crystals before and after calcined at different temperature, the surface atomic ratios are obtained from XPS spectroscopy and total atomic ratios from ICP-MS. The atomic ratios of Zr/Ti, C/Ti, P/Ti, and C/P of as-prepared and calcined samples from XPS spectroscopy are summarized in Table 4-1. As-prepared sample has lower C/P ratio of 8.14 than stoichiometric ratio of 24.0 of TOPO molecules indicating that some TOPO molecules were destroyed by high temperature during preparation process. C/P rations gradually decreases with the increase of calcination temperature below 450°C which is in agreement with the TGA result. Because the organic parts of TOPO molecules are completely removed above 550 °C, the carbon species on samples even calcined at higher temperature are mainly from environmental

pollutant.

Surface Zr/Ti ratio of samples is averagely of 0.37 which is nearly half of the stoichiometric molar ration of zirconium and titanium precursors of 0.67. However, the total Zr/Ti molar ratio of as-prepared sample examined via ICP-MS is 0.09 (See Table 4-2). Only about 10% of zirconium ions are involved in the condensation process and incorporated in the final products under this preparation condition. Actually, the heating energy of hotplate (400 °C) can only promote the preparation of TiO_2 but not high enough for ZrO_2.[15] Moreover, surface microstructure reveals higher content of zirconium than that in the bulk phase indicating that $Zr(OC_3H_7)\cdot(CH_3)_2CHOH$ reacts to TiO_2 surface after the formation of TiO_2. Zirconium precursors reveals lower reaction rate under this experimental condition than that of titanium precursors leading to the fact that most of the zirconium are incorporated on the surface layer of TiO_2. Therefore, zirconium ions mainly distributes in surface matrix of TiO_2 with low concentration in the final product.

As-prepared and calcined samples have similar average ratio of P/Ti of 0.5 presumably below temperature of 950 °C. Surface P/Ti ratio increases to 0.82 at 950 °C, mainly due to the segregation of phosphorous to surface layer. As-prepared sample has total P/Ti molar ratio of 0.022 which is also smaller than the surface ratio of 0.5 indicating that TOPO molecules react to the surface of TiO_2 with slower condensation rate than that of $TiCl_4$ under this preparation condition. Thus, phosphorous ions form TOPO molecules are mainly doped on the surface layer of TiO_2.

Since the surface and total of Zr/Ti and P/Ti molar ratios change little before and after calcination at 950 °C; calcination in air can not remove the surface phosphorous and zirconium. Moreover, heating treatment has successfully enhanced the phosphorous to higher oxidizing state and chemically bonded to surface of TiO_2 according to XPS spectroscopy. Therefore, the surface of TiO_2 can be served as modified by doping phosphorous groups and zirconium ions according to XPS and ICP-MS.

Table 4-1. Surface chemical composition of TOPO-capped Zr^{4+}/TiO_2 nanocrystals calcined at various temperatures.

Sample	AS	250	450	550	750	950
Zr/Ti	0.34	0.26	0.36	0.43	0.43	0.38
C/Ti	4.67	1.63	0.94	1.94	1.77	2.74
P/Ti	0.57	0.34	0.38	0.59	0.61	0.82
C/P	8.14	4.77	2.45	3.25	2.87	3.34

Table 4-2. Chemical compositions of TOPO-capped Zr^{4+}/TiO_2 nano-crystallites by ICP-MS analysis.

ICP-MS	Zr/Ti	P/Ti
Precursors	0.67	5.4
As-prepared	0.09	0.022
950	0.082	0.026

4-3 Microstructures

In order to examine the effect of calcination temperature on the crystalline structure, grain size and particle size, TOPO-capped Zr^{4+}/TiO_2 nano-crystals before and after calcined at different temperature were analyzed via XRD and HRTEM. Figure 4-6 displays the XRD pattern of as-prepared and calcined samples. As-prepared samples exhibit highly crystalline structures with anatase phase. This result clearly indicates that the non-hydrolytic sol-gel method can crystallize TiO_2 during synthesis. Compared with conventional sol-gel method which results in amorphous structure of as-prepared samples,R the non-hydrolytic sol-gel method provides a simple way to prepare nano-crystals without post-calcination.

No diffraction peak of ZrO_2 is observed because the zirconium ions are only served as dpants within structure of TiO_2.[15] Moreover, the diffraction of $ZrTiO_4$ phase is not observed, either. This is attributed to that the temperature for preparation is too low to crystallize $ZrTiO_4$.[12] The anatase phase exhibits special thermal stability till 950 °C. Compared Diffraction degree at 101 plane shifted from 25.2 to 25 of 2θ as calcination temperature increased to 950 °C. This indicates that the zirconium ions diffuse to the crystalline structure of TiO_2 and enlarge the d-spacing of 101 plane. The incorporation of zirconium ions has increased the strain force of TiO_2 crystalline structure. The crystalline size of the nano-crystals along the (101) plane is calculated using Scheer's equation. Table 4-3 lists the crystalline sizes of as-prepared and calcined samples at various temperatures. Grain sizes (D_{101}) increased slightly form 8.1 to 10.8 nm below 950 °C. A remarkable increase in the crystallite size from 10.2 to 16.1 nm was observed at 950 °C.
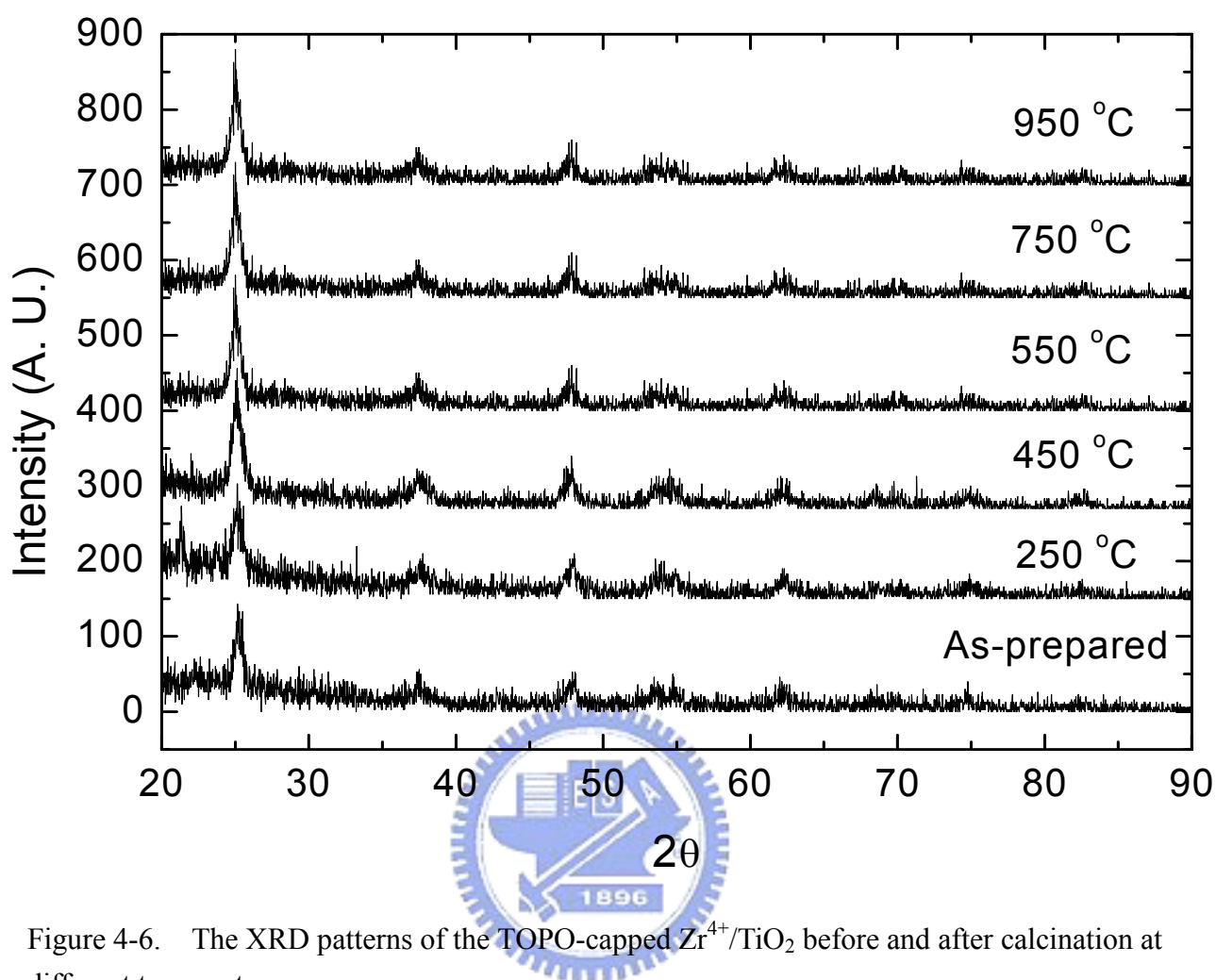
Figure 4-6. The XRD patterns of the TOPO-capped Zr^{4+}/TiO_2 before and after calcination at different temperatures.

Table 4-3. The crystallite sizes of the TOPO-capped Zr^{4+}/TiO_2 before and after calcination at different temperatures

Sample	AS-prepared	250	450	550	750	950
D_{101}	8.1	10.4	10.8	10.8	10.2	16.1

Figure 4-7 presents HRTEM pictures of as-prepared nano-crystals. Picture A displays the as-prepared nano-crystals having uniform single nano-crystalline size around 10.0 nm. Using the non-hydrolytic sol-gel method is proved to effectively synthesize uniform nano-scale size of crystallites. TOPO molecules have successfully controlled the preparation of crystallites by this non-hydrolytic sol-gel method.

The as-prepares nano-crystals are mainly composed of TiO_2 and doped with few zirconium ions and phosphorous groups; thus, as-prepared nano-crystals can be treated as single crystallites of TiO_2. Figure 4-8 displays the TOPO-capped Zr^{4+}/TiO_2 nano-crystals after calcined at various temperatures. The calicned nano-crystals below 950 °C have similar crystalline size around 10.0 nm as ell as as-prepared sample dose. The crystalline size keeps at uniform size even calcined at 750 °C is in agreement with the scale of D_{101} obtained from XRD patterns. The TOPO-capped Zr^{4+}/TiO_2 nano-crystals derived from this non-hydrolytic sol-gel method have exhibited highly thermal stability at 750 °C. However, at higher temperature of 950 °C has prompted the growth of crystals to higher size around 20 nm. Moreover, the high energy also enhances the interaction between crystalline grains with an apparently fusion interface in TEM picture.

Phosphorous and zirconium ions have been incorporated within the surface microstructure of TiO_2 nano-crystals as role of dopants. The special high thermal stability of doped-TiO_2 is significantly influenced by the dopants of P^{5+} and Zr^{4+} ions. Yang et al. has demonstrated that the incorporation of zirconium ions into TiO_2 structure can effectively retard the phase transformation of anatase to rutile form.[33] Doping of transition metal ions into TiO_2 has been proved to enhance the strength of crystal structure which is in agreement with the results observed in this reaearch.[61,62] Not only impurity of metal ions but also non-metal elements such as P and N have effective efficiency on the thermal stability of TiO_2.[2] Moreover, these impurities are the defect sites of crystalline structure of TiO_2 which have been demonstrated to inhibit the growth of crystalline size even heated at elevated

temperature.[10]   Therefore, TOPO-capped Zr^{4+}/TiO_2 has been surface doped by P and Zr ions which successfully stabilized the stability of TiO_2 from phase transformation and growth of crystallites till 950 °C.   Calcination at 950 °C provides higher energy for the crystals to break the barrier of surface phosphate and zirconium for growth and cohesion grains. Dehydroxylation or deoxygenation observed from TGA curve is suggested to promote the fusion of particles.
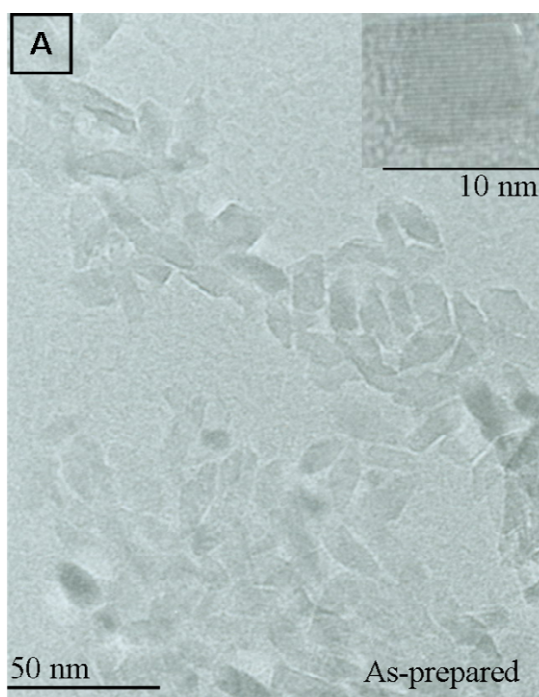
Figure 4-7.   TEM images of TOPO-capped Zr^{4+}/TiO_2 nano-crystals before calcination.

250 °C	450 °C
10 nm	10 nm

550 °C	750 °C
10 nm	10 nm

950 °C

20 nm
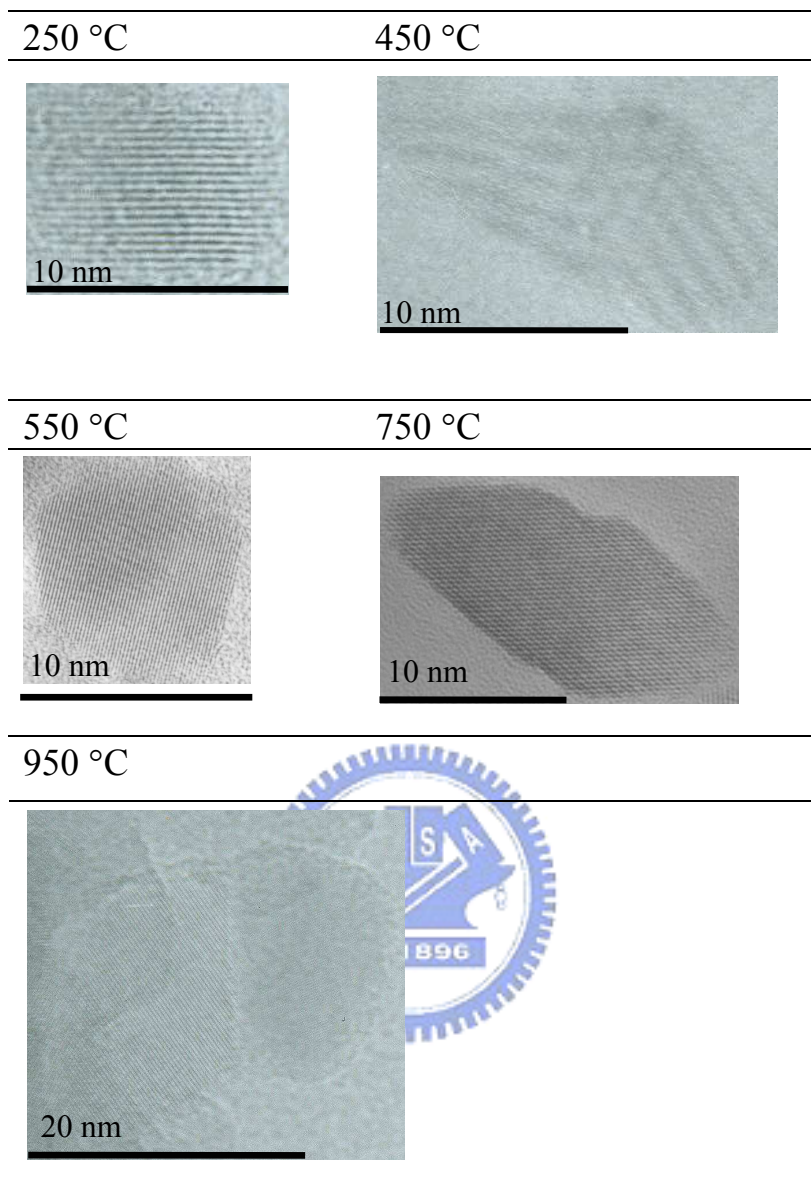
Figure 4-8.　TEM images of TOPO-capped Zr^{4+}/TiO_2 nano-crystals before calcination at various temperatures.

4-4 UV-visible absorption

In order to elucidate the optical properties for a photocatalyst, UV-visible spectroscopy was used to examine the optical reflectance of TOPO-capped Zr^{4+}/TiO_2 before and after calcined at various temperatures. Figure 4-9 illustrates the optical absorbance of TOPO-capped Zr^{4+}/TiO_2 before and after calcined at various temperatures from wavelength of 800 to 200 nm. All spectra show similar absorption behavior at an absorption edge of around 367 nm. Table 4-4 lists the band gap of as-prepared and calcined samples. The as-prepared and samples calcined at 250-750 °C have same band gap at 3.4 eV. This suggests that the as-prepared and nano-crystals calcined at 250-750 °C with quantum scale size reflecting in the band gap energy higher than bulk one of 3.2 eV. Whereas the 950°C-calcined sample has lower band gap of 3.2 eV due to the enlargement of particle size after calcined at such a high temperature. The changes of band gap energy of as-prepared and calcined nano-crystals are in agreement with the growth of crystalline size from XRD patterns.
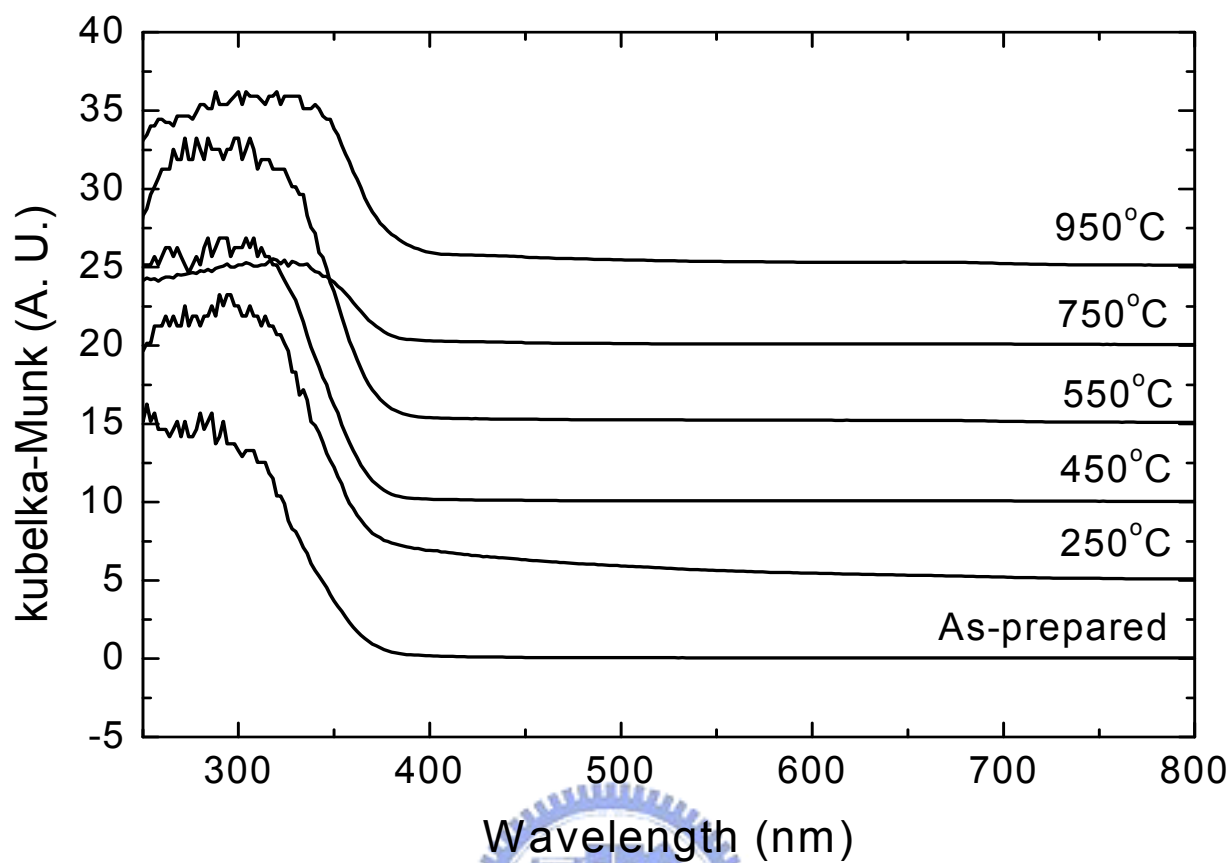
Figure 4-9. The UV-vis absorption spectra of the TOPO-capped Zr^{4+}/TiO_2 before and after calcination at different temperatures.

Table 4-4. The band gap energy of TOPO-capped Zr^{4+}/TiO_2 before and calcined at different temperature.

Sample	As-prepared	250-750	950
Band Gap (eV)	3.4	3.4	3.2

4-5   Specific Surface Area

Larger surface area can provide more active sites for reaction and enhance catalytic activity.   In order to examine the calcination effect on the surface area of nano-crystals, N_2 adsorption-desorption and BET model were carried out to calculate specific surface area, S_{BET}. Table 4-5 lists S_{BET} of as-prepared and calcined samples.   As-prepared nano-crystals had specific surface area of 0.45 m^2/g which is much lower than that of commercial P25 TiO_2 (about 50 m^2/g) due to the surface capping of TOPO molecules with higher molecular weight. Since the unit of specific surface area is surface area per unit mass of samples (m^2/g), the value of S_{BET} is ready to be adjusted by the particle size and the weight of samples.

The S_{BET} of as-prepared, 250 and 550 °C calcined samples have the tendency of decrease gradually with the increase of clacination temperature.   XRD patterns and HRTEM images reveal that the as-prepared, 250 and 550 °C calcined samples have similar particle size.   The S_{BET} of these samples are mainly altered by the weight of each sample.   TGA curve has displayed that the weight loss at 250 and 550 °C are 4% and 7% reflecting the increase of S_{BET} gradually with the increase of calcination temperature under 550 °C from 0.45 to 51.6 m^2/g.   However, the S_{BET} at 950 °C is decreased mainly caused by the enlargement of particle size (nearly 20 nm) rather than the weight loss (1%) during calcination.

Table 4-5.   The specific area of catalysts involved in RhB phtobleaching reaction.

Specific Surface Area (m^2/g)			
As-prepared	250 °C	550 °C	950 °C
0.45	28.3	51.6	2.9

4-6　Surface charge and hydrodynamic diameter of photocatalysts

Practical application of photocatalysts usually involved in aqueous system for water purification or remediation.　In order to understand the interface properties of photocatalysts in aqueous solution, the surface zeta potential and particle size distribution of mixture were examined.　Samples with evident different physicochemical properties were selected for further characterization.　According to previous results, as-prepared, 250, 550, and 950°C-calcined samples were used for subsequent characterizations.

Table 4-6 lists the pHzpc of each mixture in terms of pH value.　As-prepared nano-crystals exhibits highest isoelectric point of 5.5, and followed by 950 (pH = 5.3), 550 (pH = 3.2), and 250 (pH = 2.2).　It has been proved that the surface OH groups can obtain and lose protons with different pH value.　Surface charge is in deep relationship with the surface OH groups that higher amount of OH groups attributed to lower pHzpc.[2]　Since calcination has removed surface-capped TOPO molecules, surface of 250 and 550°C-calcined nano-crystals exhibit higher hydrophilicity with more OH groups on surface.　However, surface dehydroxylation has removed some OH groups in terms of waster leading to higher pHzpc of 950°C-calcined nano-crystals.　Some positive charge revealed on samples calcined at 950 °C indicates that dehydroxylation from surface has induced some Lewis acid sites.

Calcination under different temperature has changed the surface charge and surface Bronsted acidity which are both critical for photocatalytic activity.　Surface charge usually involved in the attraction toward target compounds for reaction; and surface Bronsted acidity always been considered as hole scavenger for produce of hydroxide radicals.[3,63,64,65]

In order to elucidate the interaction between nano-photocatalysts in RhB aqueous solution, dynamic light scattering technique was performed to determine the hydrodynamic diameter.　Table 4-7 shows the hydrodynamic diameter of catalysts dispersed in RhB aqueous solution.　250 has largest hydrodynamic diameter of 1741.83 nm and followed by 550 (1370.75 nm), 950 (939.89 nm), and as-prepared (384.88 nm).　Since RhB molecules

are ions with positive charge, surface of 250 and 550°C-calcined samples with more negative charge can effectively concentrate RhB cations on surface.[18]   The growth of particle size 0f 250 and 550°C-calcined samples compared can also induce an enlargement of hydrodynamic diameter.   At 950 °C, the surface negative charge decreases with higher pHzpc cause by dehydroxylation reducing the attachment of RhB cations.   However, the growth of crystallites and cohesion between particles also enhances the hydrodynamic diameter of nano-crystals calcined at 950 °C in RhB aqueous solution.   As-prepared nao-crystals have less negative charge and smaller particle size that the hydrodynamic diameter is much smaller than calcined nano-crystals.

Table 4-6.   Surface zero point charge of TOPO-capped Zr^{4+}/TiO_2 nano-crystals before and after calcined at different temperature.

Sample	As-prepared	250 °C	550 °C	950 °C
pHzpc	5.5	2.2	3.2	5.3

Table 4-7.   Particle size distribution of TOPO-capped Zr^{4+}/TiO_2 nano-crystals before and after calcined at different temperature in RhB solution.

	As-prepared	250 °C	550 °C	950 °C
Hydrodynamic diameter (nm)	385	1742	1371	940

4-7 Photocatalytic activity

The photocatalytic activity of TOPO-capped Zr^{4+}/TiO_2 nano-crystals before and after calcined at different temperatures was examined by regarding the decoloration of RhB monitored at 553 nm. Commercial TiO_2 of Degussa P25 was also taken for photocatalytic test as a comparison. Figure 4-10 shows the photocatalytic activity of as-prepared and calcined TOPO-capped Zr^{4+}/TiO_2 in terms of the change of RhB concentration as a function of illumination time. In the absence of photocatalysts, RhB was stable when illuminated at UV light of 305 nm. The degradation of RhB in the presence of photocatalysts indicates that all photocatalysts prepared in this study exhibited photocatalytic activity. The photodecomposition of RhB followed pseudo-first-order kinetics. Table 4-8 lists the degradation rate constant (min^{-1}) and specific degradation rate constant ($min^{-1}m^{-2}g$) of TOPO-capped Zr^{4+}/TiO_2 nano-crystals and P25.

Among as-prepared and calcined samples, the photocatalysts calcined at 550 °C exhibited the highest apparent decoloration rate ($k = 5.9 \times 10^{-2}$ min^{-1}), and followed by calcination at 250 °C ($k = 5.7 \times 10^{-2}$ min^{-1}), as-prepared ($k = 4.9 \times 10^{-2}$ min^{-1}) and calcination at 950 °C ($k = 1.9 \times 10^{-2}$ min^{-1}).

However, as-prepared sample has the highest intrinsic photoactivities ($k = 0.11$ $g \cdot m^{-2} \cdot min^{-1}$) followed by 950 ($k = 6.6 \times 10^{-3}$ $g \cdot m^{-2} \cdot min^{-1}$), P25 ($k = 2.8 \times 10^{-3}$ $g \cdot m^{-2} \cdot min^{-1}$), 250 ($k = 2.0 \times 10^{-3}$ $g \cdot m^{-2} \cdot min^{-1}$), and 550 ($k = 1.2 \times 10^{-3}$ $g \cdot m^{-2} \cdot min^{-1}$) when normalized to the specific surface area.
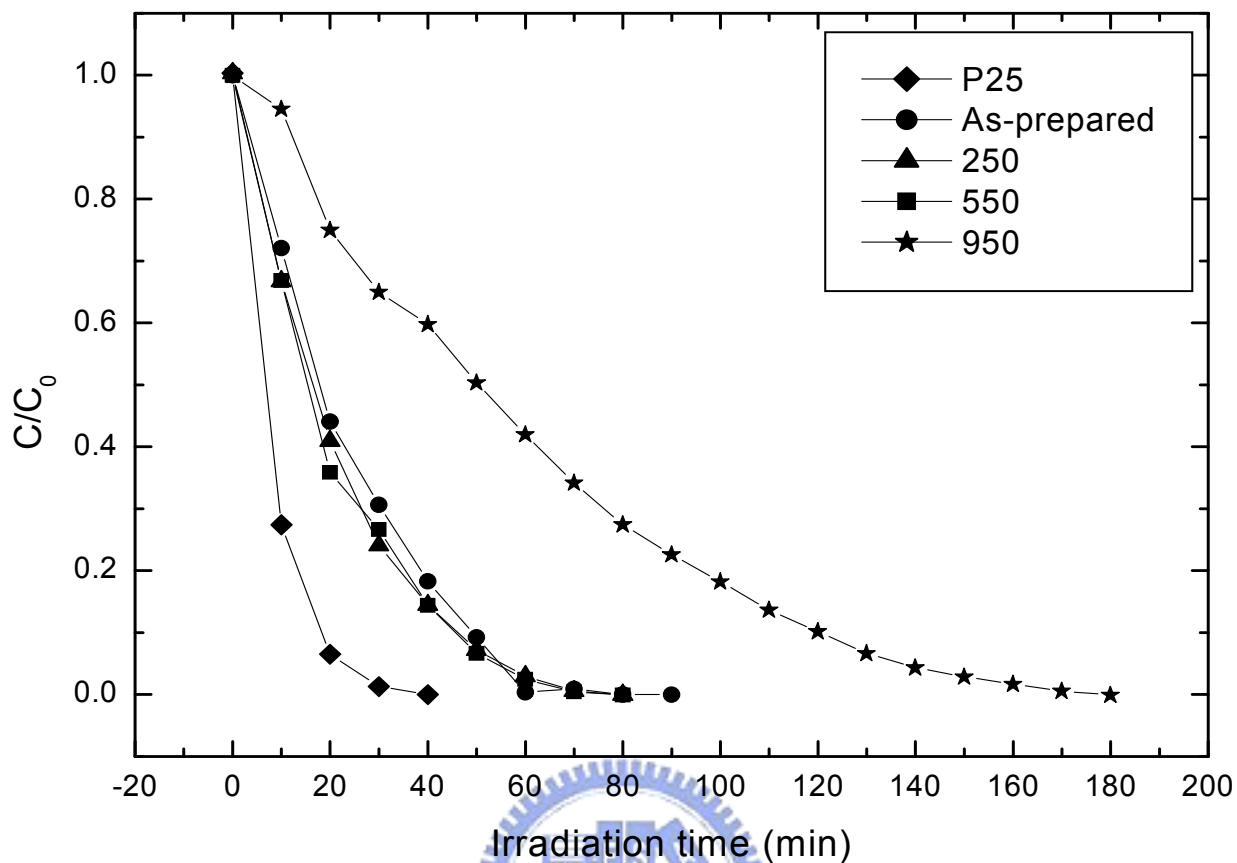
Figure 4-10.　The decoloration of RhB by TOPO–capped Zr^{4+}/TiO_2 before and after calcined

at different temperature compared with P25.

Table 4-8.　Photocatalytic activity of TOPO-capped Zr^{4+}/TiO_2 before and after calcination at

different temperature on decoloration of RhB and compared with P25.

Sample	P25	As-prepared	250 °C	550 °C	950 °C
Degradaiton rate constant (min^{-1})	0.141	4.9×10^{-2}	5.7×10^{-2}	5.9×10^{-2}	1.9×10^{-2}
Specific photocatalytic activity (g·min^{-1}·m^{-2})	2.8×10^{-3}	0.11	2.0×10^{-3}	1.2×10^{-3}	6.6×10^{-3}

Since all the calcined nano-crystals exhibit anatase form and similar band gaps (3.4-3.2 eV); it is suggested that the surface chemical compositions influence dominantly on the photoactivities rather than the structural properties do.

Surface acidification of TiO_2 has been demonstrated to improve the photocatalytic activities of TiO_2.[2,66]   In this study, calcination at 250 and 550°C shown high surface acidity due to formation of P-OH groups from the oxidation of TOPO molecules and calcination at 950°C presented Lewis acidity because of dehydroxylation.   Korosi et al. has demonstrated that the concentration of phosphorous influenced the physicochemical properties of TiO_2 and photoactivities.   P/Ti molar ratio of 0.01 has been proven the optimal concentration for TiO_2 on the oxidation of phenol compounds.   Since the total P/Ti molar ratios of as-prepared and nano-crystals calcined at 950 °C are very close indicating that calcinaiton can not remove the phosphorous groups from Zr^{4+}/TiO_2 prepared by the non-hydrolytic sol-gel method.   The samples calcined at 250 and 550 °C should have similar content of phosphorous of P/Ti = 0.022-0.026 which is close to the optimal value of 0.01 in Korosi's research.   Thus, the phosphated Zr^{4+}/TiO_2 nano-crystals contain a proper molar ratio of P/Ti and the photocatalytic activities are ready to be controlled by calcinations temperature.

Moreover, surface P/Ti ratio also plays an important role in photoactivities.   In order to elucidate the content of surface P/Ti molar ratio on the decoloration of RhB dyes, phosphated P25 (denoted as PP25) prepared by pregnant in different concentration of phosphoric acid was carried out to test the photoactivities.   The detail results and discussion of PP25-M (M denotes as concentration of phosphoric acid) are presented in Appendix B.   As observed, the optimal content of surface P/Ti molar ratio of PP25 is 0.72 (Appendix B-4) which is similar to that of as-prepared and calcined nano-crystals (average value = 0.58).   These results indicate that the nano-crystals derived from the non-hydrolytic sol-gel route have both proper total and surface P/Ti molar ratios even calcined at 950 °C.   As a consequence, the proper

surface Bronsted acidity has been the effective factor to enhance the photoacticities of nano-crystals calcined 250 and 550 °C toward the decoloration of RhB dyes.

Although calcination at 550 °C presented high apparent degradation rate, it has higher surface area than those of as-prepared and nano-crystals calcined at 250 and 950 °C. The amounts of surface active sites per gram of samples are different due to the difference in specific surface area. In order to evaluate how surface properties affect photoactivities, the apparent degradation rate is normalized to specific surface area. Thus, the main factor which deeply influences the photoactivities is the surface chemical composition of each photocatalyst.

As-prepared samples exhibit the highest intrinsic rate which indicating that modification with organic compounds improves the photoactivity more obviously than inorganic compounds dose. This is also in agreement with the difference between samples calcined at 250 and 550 °C that the residual carbonaceous groups of C=O, O-C=O, and C-C from surface TOPO molecules at 250 °C provide higher activity than the oxidized phosphate groups of P-OH.

Calcination at 950 °C induces a more active surface chemical species which exhibit higher surface activity than that of samples calcined at 250 and 550 °C. Dehydroxylation at 950 °C turns surface more positive charges with surface acid species of Lewis acid site and phosphate species of P=O. These surface species exhibit higher activity than Bronsted acid site and P-OH species at 550 °C which displays a different phenomenon from other research. Moreover, samples calcined at 950 °C also exhibit higher intrinsic activity than P25 though some properties are different.

Chapter 5.   Conclusions

Zr-doped anatase TiO_2 nano-crystals have been successfully synthesized through a nonhydrolytic sol-gel process when TOPO is used as solvent and chelating agents as well. The nano-crystals were chemically capped with TOPO and exhibited hydrophocility. Calcination process changes the crystallite sizes and surface properties including hydrophibility, compositions, speciation and functional groups of the as-prepared samples and so as the photoactivities.   After removal of the organic part of TOPO at 300-550 °C, the surface turns from phodrophobic to hydrophilic.   Moreover, P^{5+} was incorporated into surface lattice of the nano-crystals.   The co-incorporation of Zr^{4+} and P^{5+} enhanced the thermal stability and maintained band gap till 950 °C.   Phosphorous head groups were oxidized to different phosphate moiety at different temperature.   In addition, dehydroxylation at higher temperature changes the types of acid from Bronsted acid to Lewis one.

Zr^{4+}/TiO_2 nao-crystals calcined at 550 °C with higher surface area, Bronsted acidity, and adsorption capacity of RhB, therefore exhibited the highest apparent degradation rate toward the decoloration of RhB.   The intrinsic photoactivities are ranked as the order of as-prepared samples > Zr^{4+}/TiO_2 nao-crystals calcined at 950 °C > Zr^{4+}/TiO_2 nao-crystals calcined at 250 °C > Zr^{4+}/TiO_2 nao-crystals calcined at 550 °C.   Surface modifier, acid types and functional groups dominant the surface photoactivities of TiO_2.   Lewis acidity and P=O functional group greatly promote the surface photoactives followed by organic modifier and Bronsted acidity.   The influence of surface Lewis acid site and P=O on the mechanism and dynamics of photocatalysts requires further investigation to better understand the photocatalytic chemistry.

References

(1) Brune, A.; Jeong, G. J.; Liddell, P. A.; Sotomura, T.; Moore, T. A.; Moore, A. L.; Gust, D. *Langmuir*

Langmuir **2004**, *20*, 8366.

(2) Yamashita, H.; Nishida, Y.; Yuan, S.; Mori, K.; Narisawa, M.; Matsumura, Y.; Ohmichi, T.; Katayama, I. *Catal. Today* **2007**, *120*, 163.

(3) Bahnemanna, D. W.; Kholuiskaya, S. N.; Dillert, R.; Kulak, A. I.; Kokorin, A. I. *Appl Catal B-Environ*

Appl Catal B-Environ **2002**, *36*, 161.

(4) Das, D.; Chakrabarty, D. K. *Energ Fuel*

Energ Fuel **1998**, *12*, 109.

(5) Fu, X. Z.; Clark, L. A.; Yang, Q.; Anderson, M. A. *Environ Sci Technol*

Environ Sci Technol **1996**, *30*, 647.

(6) Kapoor, M. P.; Inagaki, S.; Yoshida, H. *J Phys Chem B*

J Phys Chem B **2005**, *109*, 9231.

(7) Tan, S. S.; Zou, L.; Hu, E. *Catal. Today* **2006**, *115*, 269.

(8) Stone, V. F.; Davis, R. J. **1998**, *10*, 1468.

(9) Huang, L. M.; Li, Q. Z. *Chem Lett*

Chem Lett **1999**, 829.

(10) Korosi, L.; Dekany, I. **2006**, *280*, 146.

(11) Vioux, A. *Chem Mater*

Chem Mater **1997**, *9*, 2292.

(12) Andrianainarivelo, M.; Corriu, R. J. P.; Leclercq, D.; Mutin, P. H.; Vioux, A. *J Mater Chem*

J Mater Chem **1997**, *7*, 279.

(13) Trentler, T. J.; Denler, T. E.; Bertone, J. F.; Agrawal, A.; Colvin, V. L. *J Am Chem Soc*

J Am Chem Soc **1999**, *121*, 1613.

(14) Joo, J.; Yu, T.; Kim, Y. W.; Park, H. M.; Wu, F. X.; Zhang, J. Z.; Hyeon, T. *J Am Chem Soc*

J Am Chem Soc **2003**, *125*, 6553.

(15) Chang, S. M.; Doong, R. A. *Chemosphere* **2006**, *62*, 1869.

(16) Linsebigler, A. L.; Lu, G. Q.; Yates, J. T. **1995**, *95*, 735.

(17) Cozzoli, P. D.; Kornowski, A.; Weller, H. **2003**, *125*, 14539.

(18) Wu, T. X.; Liu, G. M.; Zhao, J. C.; Hidaka, H.; Serpone, N. **1998**, *102*, 5845.

(19) Galanfereres, M.; Alemany, L. J.; Mariscal, R.; Banares, M. A.; Anderson, J. A.;

Fierro, J. L. G. **1995**, *7*, 1342.

(20) Wu, L.; Yu, J. C.; Fu, X. Z. **2006**, *244*, 25.

(21) Takagaki, A.; Sugisawa, M.; Lu, D. L.; Kondo, J. N.; Hara, M.; Domen, K.; Hayashi, S. **2003**, *125*, 5479.

(22) Pathak, P.; Meziani, M. J.; Castillo, L.; Sun, Y. P. *Green Chem.* **2005**, *7*, 667.

(23) Imanishi, A.; Tsuji, E.; Nakato, Y. **2007**, *111*, 2128.

(24) Shammugam, S.; Gabashvili, A.; Jacob, D. S.; Yu, J. C.; Gedanken, A. **2006**, *18*, 2275.

(25) Ou, Y.; Lin, J. D.; Zou, H. M.; Liao, D. W. **2005**, *241*, 59.

(26) Choi, W. Y.; Termin, A.; Hoffmann, M. R. **1994**, *98*, 13669.

(27) Wang, L. G.; Pennycook, S. J.; Pantelides, S. T. *Phys. Rev. Lett.* **2002**, *89*.

(28) Arabatzis, I. M.; Stergiopoulos, T.; Andreeva, D.; Kitova, S.; Neophytides, S. G.; Falaras, P. *J Catal*

J Catal **2003**, *220*, 127.

(29) Van Gestel, T.; Van der Bruggen, B.; Buekenhoudt, A.; Dotremont, C.; Luyten, J.; Vandecasteele, C.; Maes, G. *J Membrane Sci*

J Membrane Sci **2003**, *224*, 3.

(30) Mor, G. K.; Shankar, K.; Paulose, M.; Varghese, O. K.; Grimes, C. A. *Nano Lett*

Nano Lett **2006**, *6*, 215.

(31) Sibu, C. P.; Kumar, S. R.; Mukundan, P.; Warrier, K. G. K. **2002**, *14*, 2876.

(32) Guidi, V.; Carotta, M. C.; Ferroni, M.; Martinelli, G.; Sacerdoti, M. **2003**, *107*, 120.

(33) Yang, J.; Ferreira, J. M. F. **1998**, *33*, 389.

(34) Cong, Y.; Zhang, J. L.; Chen, F.; Anpo, M. **2007**, *111*, 6976.

(35) Konishi, J.; Fujita, K.; Nakanishi, K.; Hirao, K. *Chem Mater*

Chem Mater **2006**, *18*, 6069.

(36) Calleja, G.; Serrano, D. P.; Sanz, R.; Pizarro, P.; Garcia, A. *Ind Eng Chem Res*

Ind Eng Chem Res **2004**, *43*, 2485.

(37) Tao, Y.; Wu, C. Y.; Mazyck, D. W. *Ind Eng Chem Res*

Ind Eng Chem Res **2006**, *45*, 5110.

(38) Torimoto, T.; Okawa, Y.; Takeda, N.; Yoneyama, H. *J Photoch Photobio A*

J Photoch Photobio A **1997**, *103*, 153.

(39) Nagaoka, S.; Hamasaki, Y.; Ishihara, S.; Nagata, M.; Iio, K.; Nagasawa, C.; Ihara, H. **2002**, *177*, 255.

(40) Takeda, N.; Torimoto, T.; Sampath, S.; Kuwabata, S.; Yoneyama, H. **1995**, *99*, 9986.

(41) Rajh, T.; Nedeljkovic, J. M.; Chen, L. X.; Poluektov, O.; Thurnauer, M. C. **1999**, *103*, 3515.

(42) Pal, B.; Torimoto, T.; Iwasaki, K.; Shibayama, T.; Takahashi, H.; Ohtani, B. *J Phys*

Chem B

J Phys Chem B **2004**, *108*, 18670.

(43) Rogach, A. L.; Kornowski, A.; Gao, M. Y.; Eychmuller, A.; Weller, H. *J Phys Chem B*

J Phys Chem B **1999**, *103*, 3065.

(44) Zheng, S.; Gao, L. A.; Zhang, Q. H.; Guo, J. K. **2000**, *10*, 723.

(45) Zhang, J. L.; Hu, Y.; Matsuoka, M.; Yamashita, H.; Minagawa, M.; Hidaka, H.; Anpo, M. **2001**, *105*, 8395.

(46) Colon, G.; Sanchez-Espana, J. M.; Hidalgo, M. C.; Navio, J. A. **2006**, *179*, 20.

(47) Bhaumik, A.; Inagaki, S. **2001**, *123*, 691.

(48) Jones, D. J.; Aptel, G.; Brandhorst, M.; Jacquin, M.; Jimenez-Jimenez, J.; Jimenez-Lopez, A.; Maireles-Torres, P.; Piwonski, I.; Rodriguez-Castellon, E.; Zajac, J.; Roziere, J. **2000**, *10*, 1957.

(49) Zhao, J. C.; Wu, T. X.; Wu, K. Q.; Oikawa, K.; Hidaka, H.; Serpone, N. **1998**, *32*, 2394.

(50) Vohra, M. S.; Tanaka, K. **2001**, *35*, 411.

(51) Wong, M. S.; Antonelli, D. M.; Ying, J. Y. **1997**, *9*, 165.

(52) Hench, L. L.; West, J. K. *Chem Rev*

Chem Rev **1990**, *90*, 33.

(53) Andrianainarivelo, M.; Corriu, R. J. P.; Leclercq, D.; Mutin, P. H.; Vioux, A. **1997**, *9*, 1098.

(54) Andrianainarivelo, M.; Corriu, R. J. P.; Leclercq, D.; Mutin, P. H.; Vioux, A. **1997**, *8*, 89.

(55) Arnal, P.; Corriu, R. J. P.; Leclercq, D.; Mutin, P. H.; Vioux, A. **1997**, *9*, 694.

(56) Yahaya, A. H.; Gondal, M. A.; Hameed, A. *Chem. Phys. Lett.* **2004**, *400*, 206.

(57) Zhang, M.; Gao, G.; Zhao, D. C.; Li, Z. Y.; Liu, F. Q. **2005**, *109*, 9411.

(58) Lacombe, S.; Cardy, H.; Soggiu, N.; Blanc, S.; Habib-Jiwan, J. L.; Soumillion, J. P. **2001**, *46*, 311.

(59) Yang, J.; Juan, P.; Shen, Z. M.; Guo, R.; Jia, J. P.; Fang, H. J.; Wang, Y. L. **2006**, *44*, 1367.

(60) Gomez, R.; Lopez, T.; Tzompantzi, F.; Garciafigueroa, E.; Acosta, D. W.; Novaro, O. **1997**, *13*, 970.

(61) Reddy, B. M.; Sreekanth, P. M.; Reddy, E. P.; Yamada, Y.; Xu, Q. A.; Sakurai, H.; Kobayashi, T. **2002**, *106*, 5695.

(62) Reddy, B. M.; Ganesh, I. **2001**, *169*, 207.

(63) Vohra, M. S.; Kim, S.; Choi, W. **2003**, *160*, 55.

(64) Park, H.; Choi, W. **2005**, *109*, 11667.

(65) Yang, Q. J.; Xie, C.; Xu, Z. L.; Gao, Z. M.; Du, Y. G. **2005**, *109*, 5554.

(66) Kabra, K.; Chaudhary, R.; Sawhney, R. L. **2004**, *43*, 7683.

Appendix A.   Experimental parameters

Appendix A-1.   Operational parameters of TGA/DSC

	Start ℃	Limit ℃	Atmosphere	Rate ℃/min	Air Flow mL/min
TGA	RT	1000	Air	10	50
DSC	RT	1000	Air	10	50

Appendix A-2.   Operational parameters of XPS.

Mode	Binding energy	Pass energy	Anode	Step size	Time/steps
Survey	1200-0 eV	23.5 eV	Al	1.0 eV	50 ms
Multiplex	Depending on element	23.5 eV	Al	0.1 eV	50 ms

Appendix A-3.   Detail operational parameters of XPS in multiplex.

Element	Pass energy	Step isze	Scans	BE range	ASF
O 1s	23.5	0.1 eV	30	525-545	0.711
P 2p	23.5	0.1 eV	80	127-147	0.486
Ti 2p	23.5	0.1 eV	25	451-476	2.001
Zr 3d	23.5	0.1 eV	40	174-194	2.576
C 1s	23.5	0.1 eV	40	280-300	0.296

Appendix A-4.　Operational parameters of FT-IR

Parmeter	Scans	Resolution	Gain	Range cm^{-1}	TYPE	Scan speed
P	100	4	Auto	800-1300	ABS	5
Total	100	4	Auto	400-4000	ABS	5

Appendix A-5.　Operational parameters of XRPD

Scan range (degree)	Sampling Width (degree)	San Speed (degree/min)	Measurement type	Voltage (kV)	Current (mA)
20-90 degree (2-120)	0.02	4.0	Ordinary (without background)	30.0	20.0
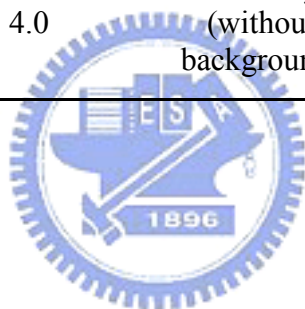
Appendix A-6.　Operational parameters of UV-visible.

Measurement	Data Mode	Starting Wavelength	Ending Wavelength	Sampling Interval	Slit Width	Reference
Wavelength scan	%R	800 nm	200 nm	1 nm	1 nm	Al_2O_3
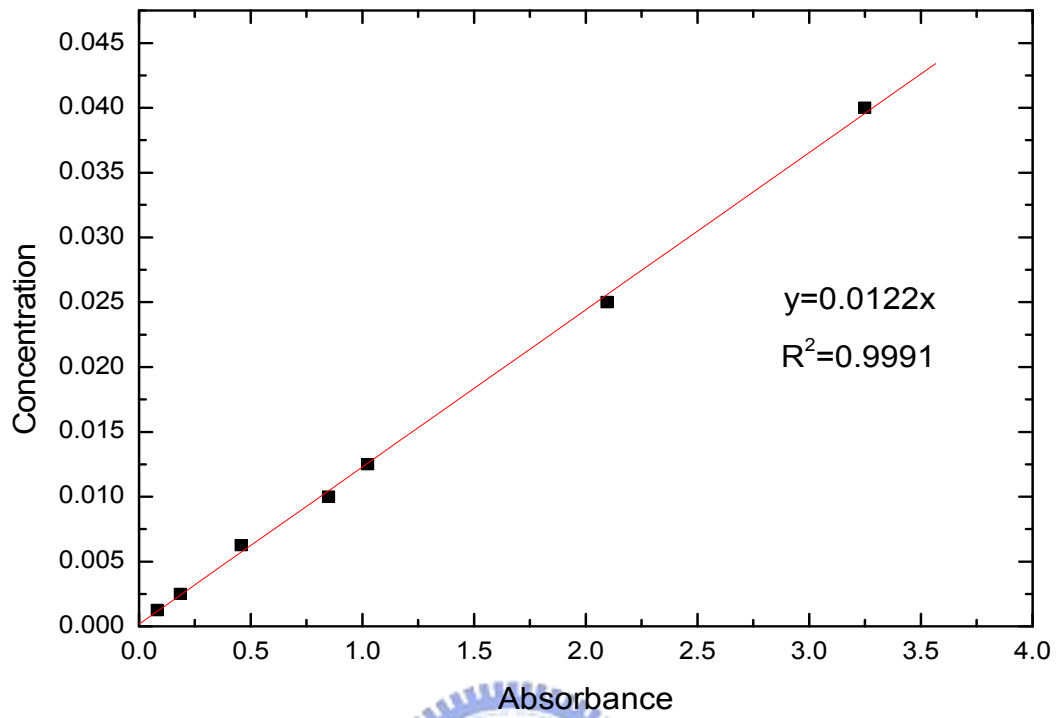
Appendix A-4.　Calibration curve of RhB aqueous solution.

Appendix B.   Low-magnification TEM images
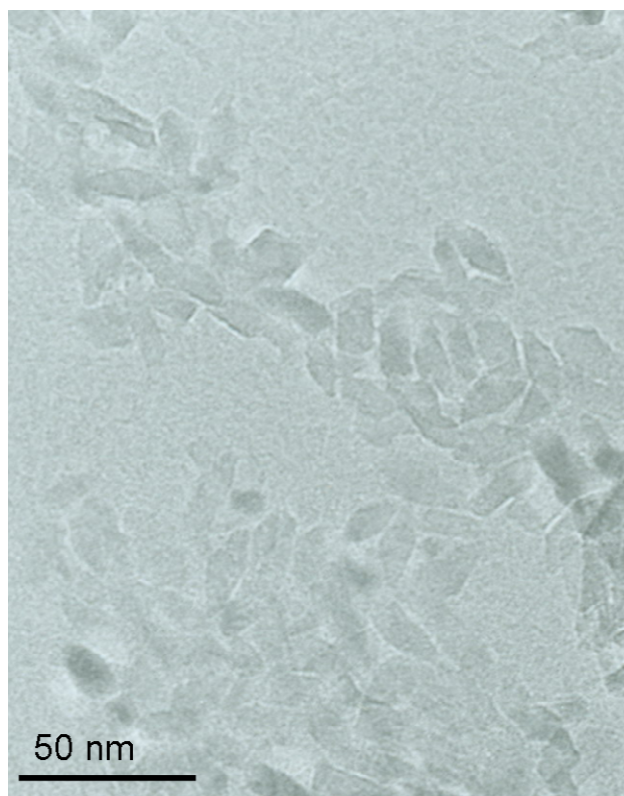
Appendix B-1.　Low-magnification TEM image of as-prepared Zr^{4+}/TiO_2 nano-crystals.

50 nm
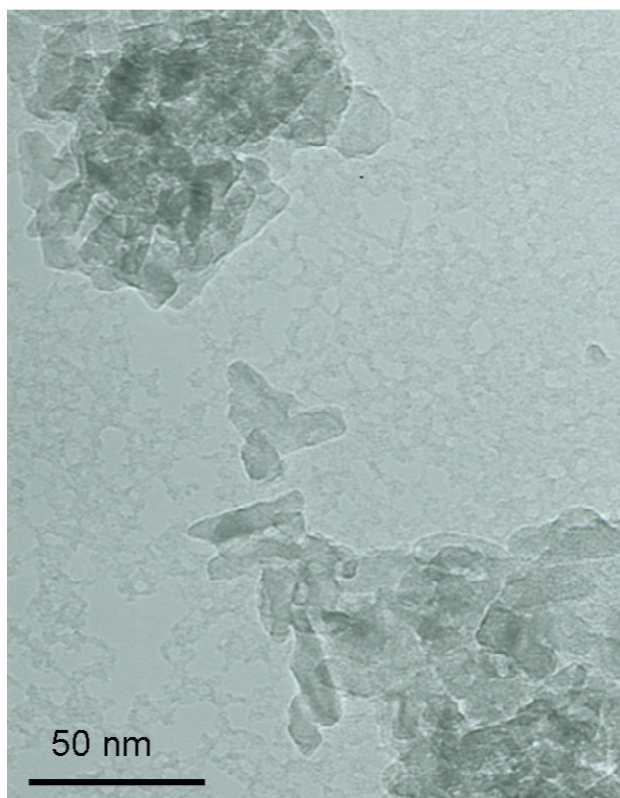
Appendix B-2.   Low-magnification TEM image of Zr^{4+}/TiO_2 nano-crystals calcined at 250°C
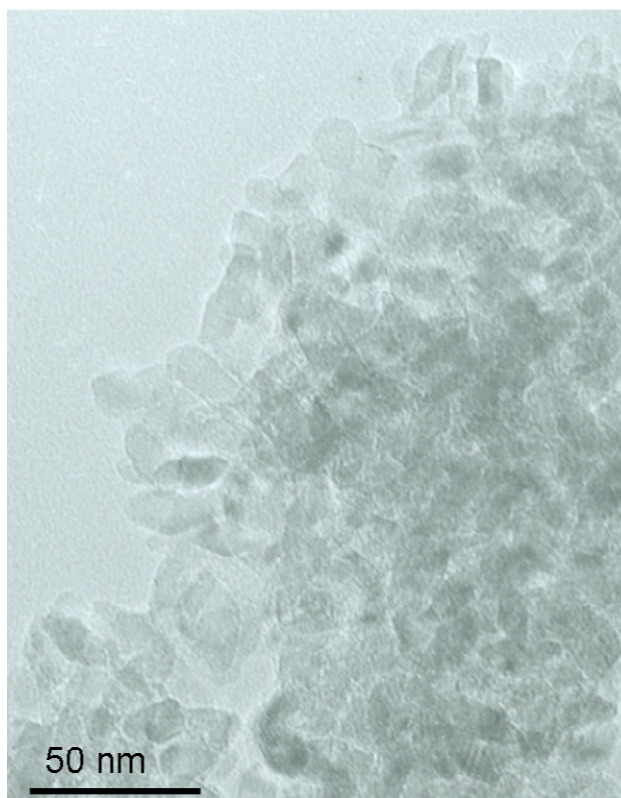
Appendix B-3.   Low-magnification TEM image of Zr^{4+}/TiO$_2$ nano-crystals calcined at 450°C

50 nm
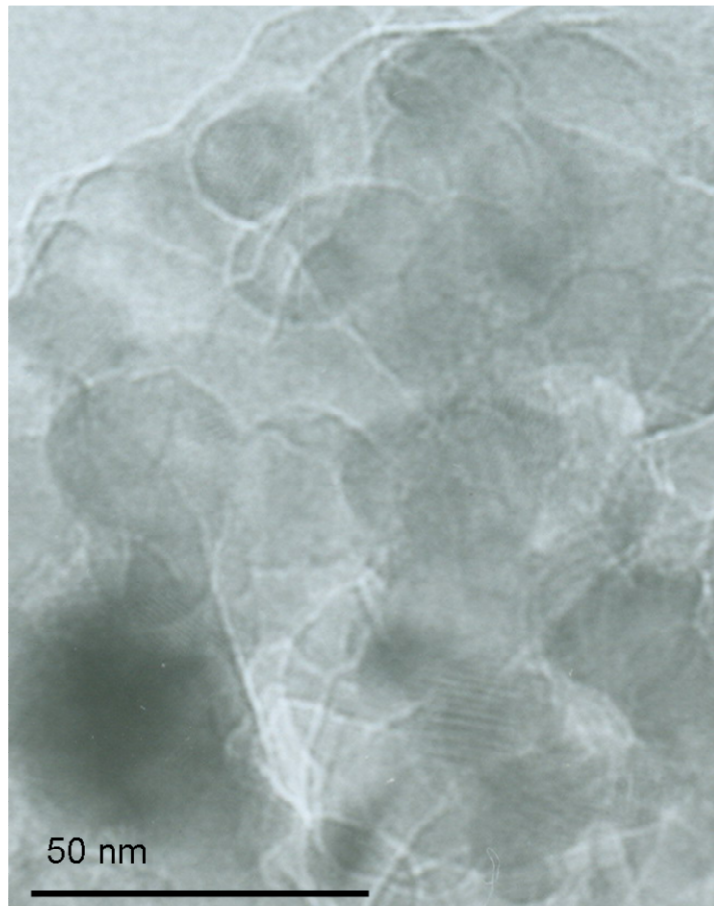
Appendix B-4.   Low-magnification TEM image of Zr^{4+}/TiO_2 nano-crystals calcined at 950°C

Appendix C.   Zeta potential as a function of pH
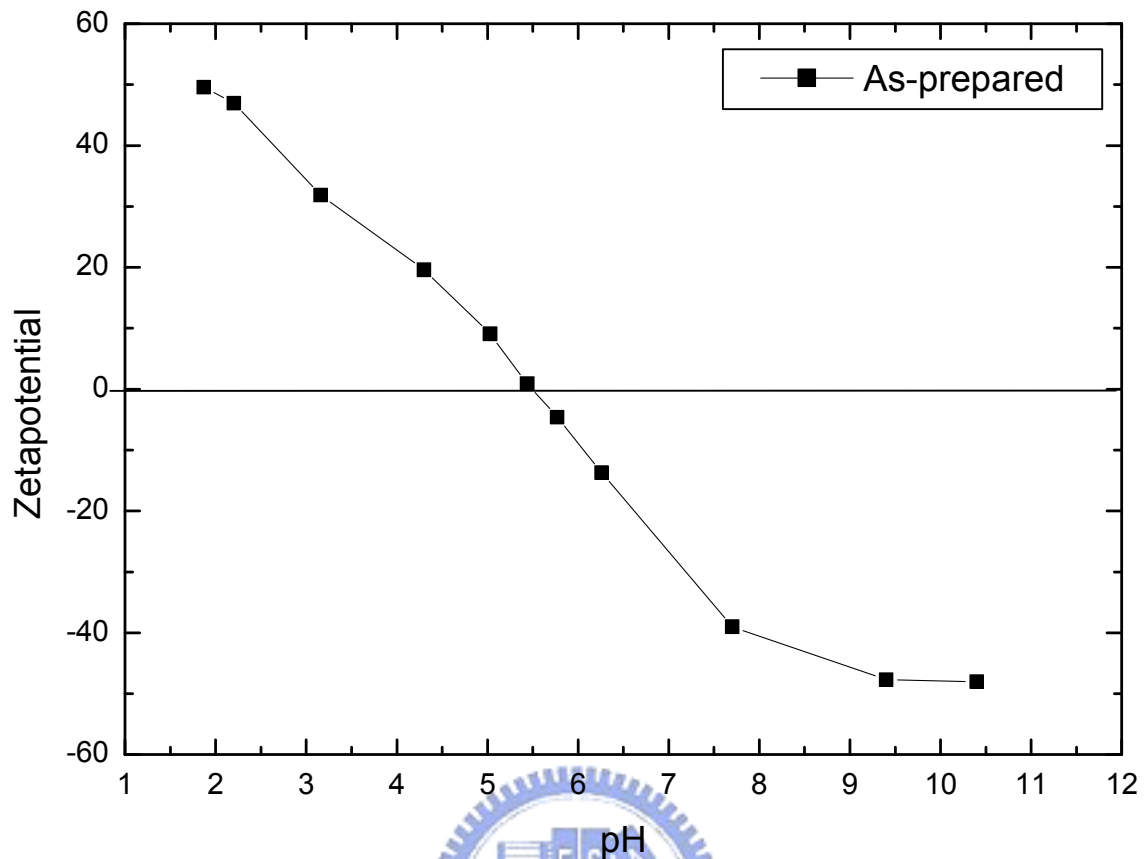
Appendix C-1.   Zetapotential as a function of pH of as-prepared samples
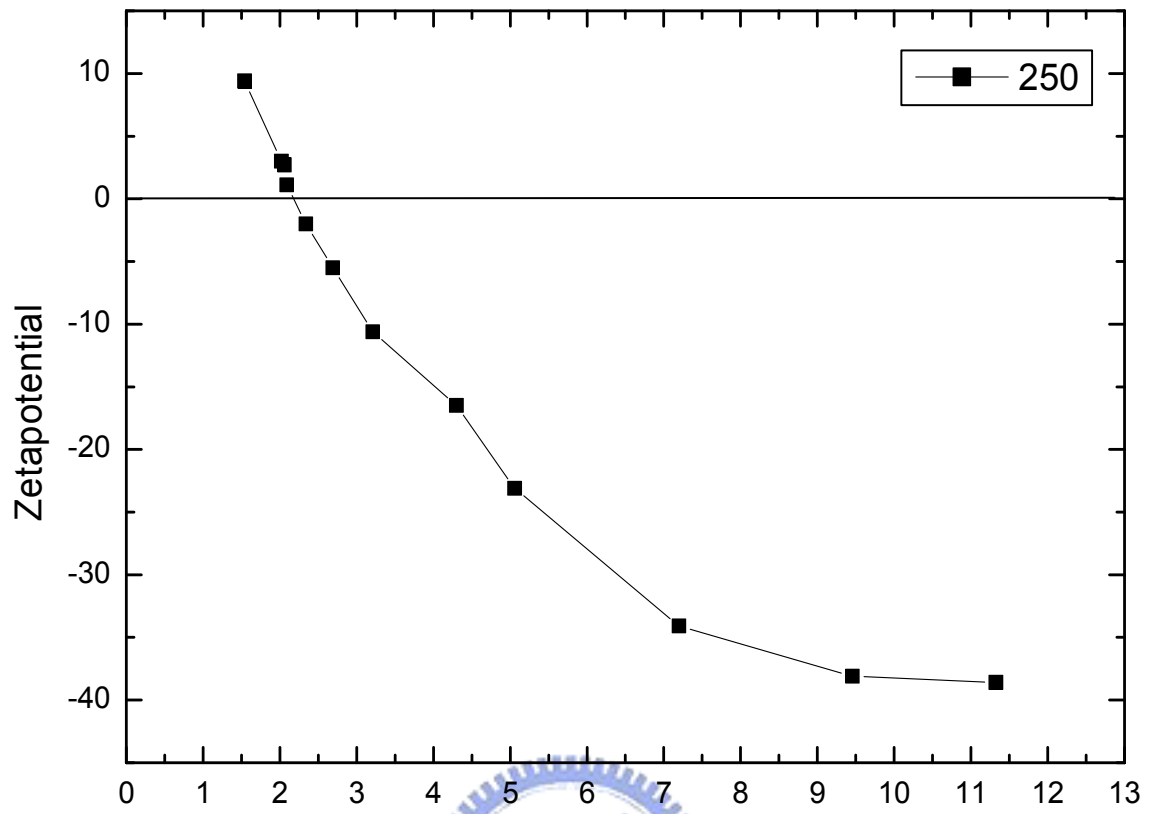
Appendix C-2.　Zetapotential as a function of pH of samples calcined at 250 °C.
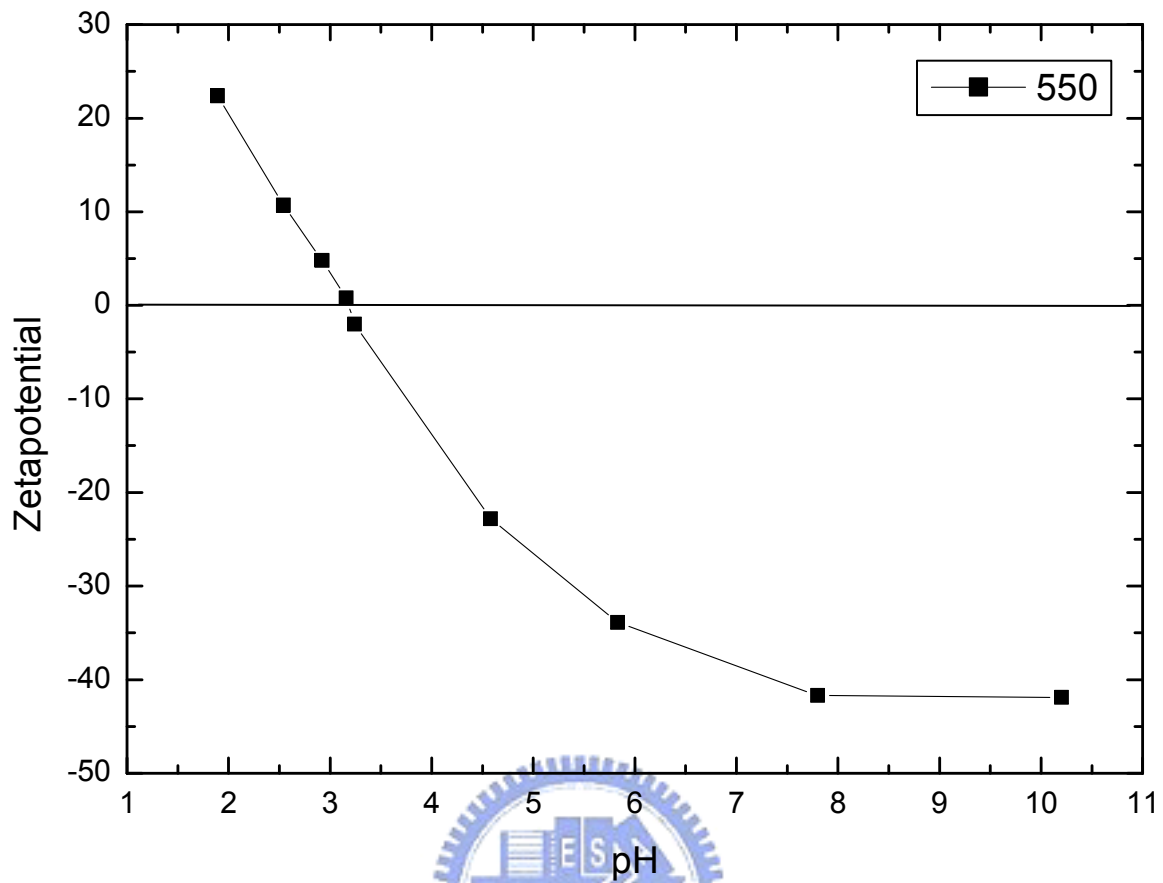
Appendix C-3.   Zetapotential as a function of pH of samples calcined at 550 °C.
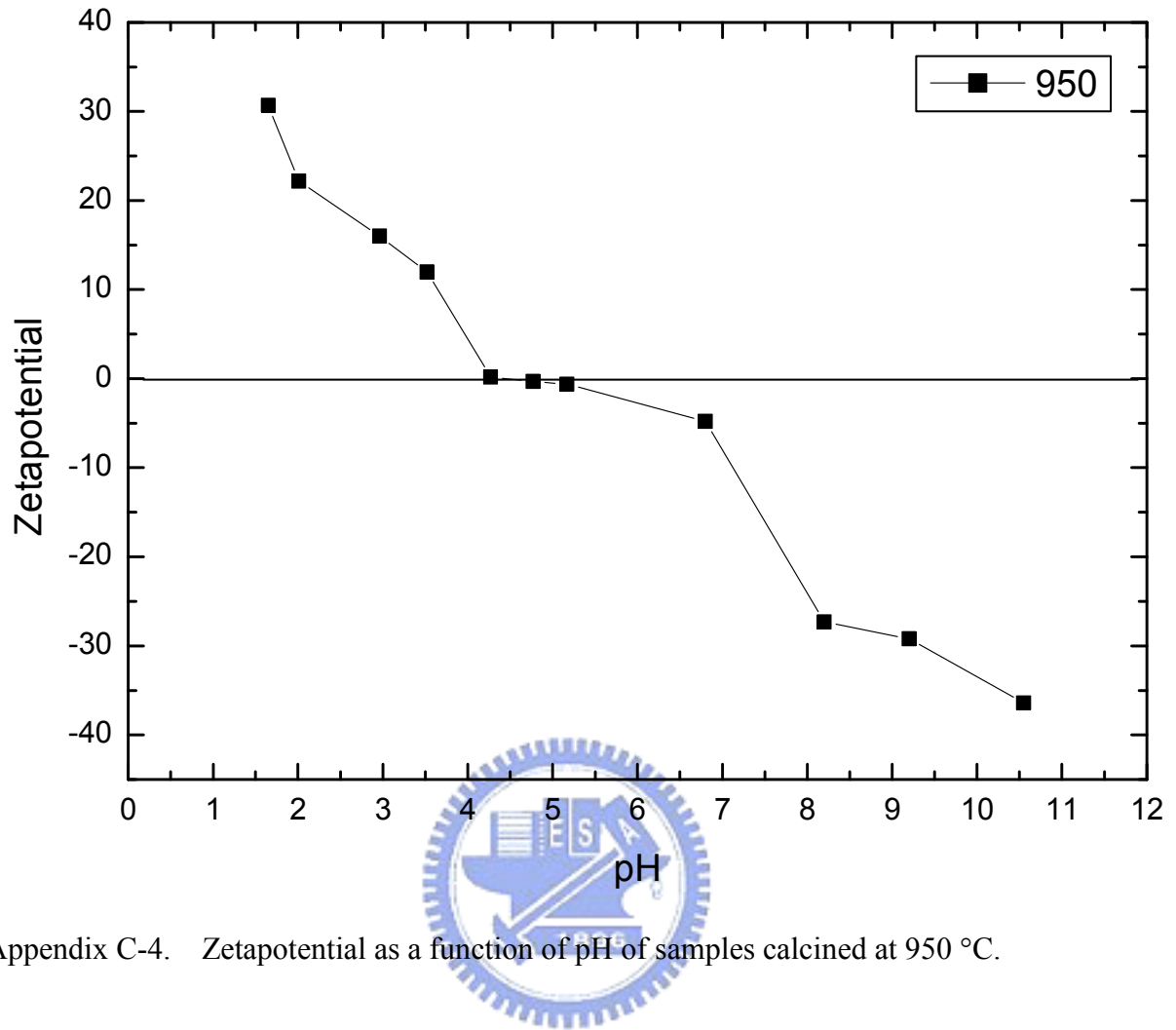
Appendix C-4.   Zetapotential as a function of pH of samples calcined at 950 °C.
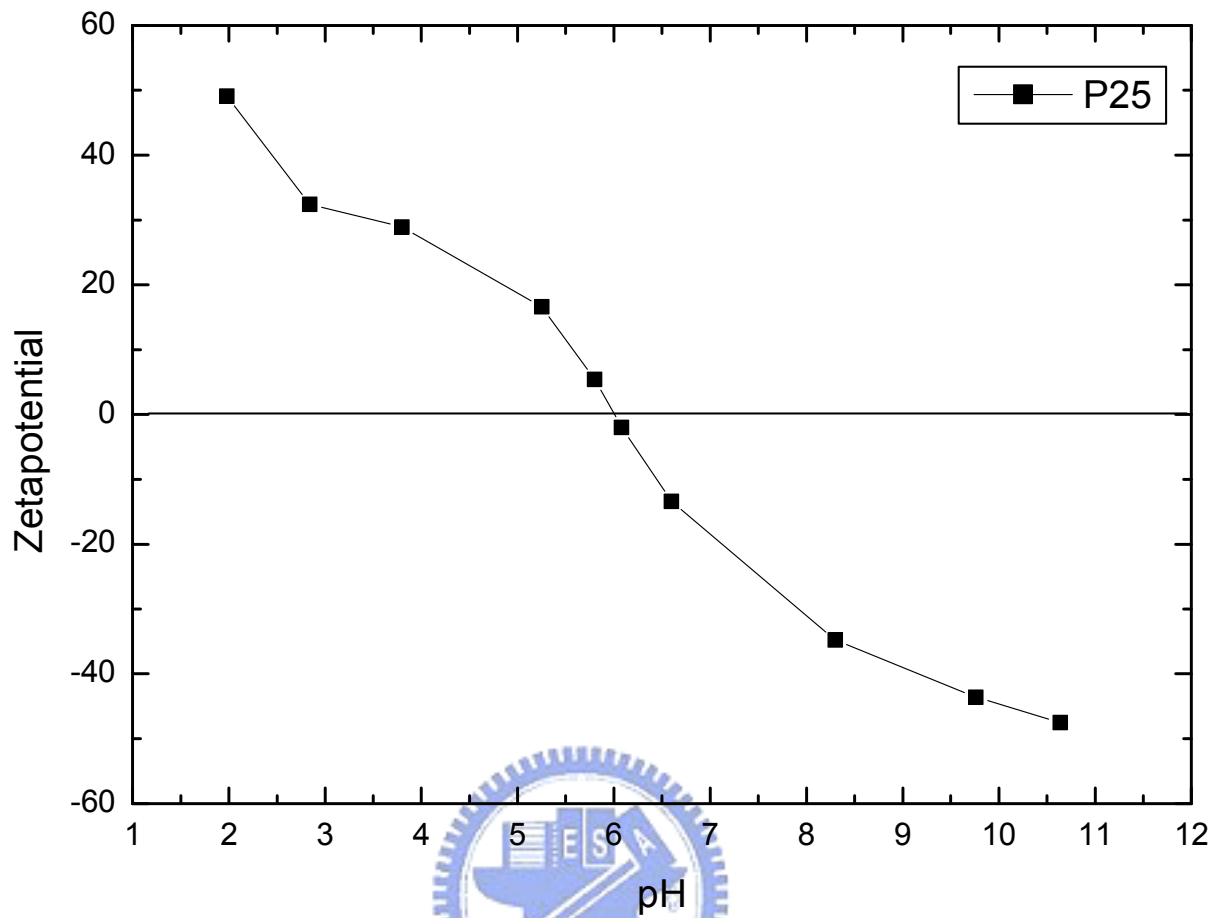
Appendix C-5.   Zetapotential as a function of pH of Degussa P25.

Appendix D.   Distribution of hydrodynamic diameter

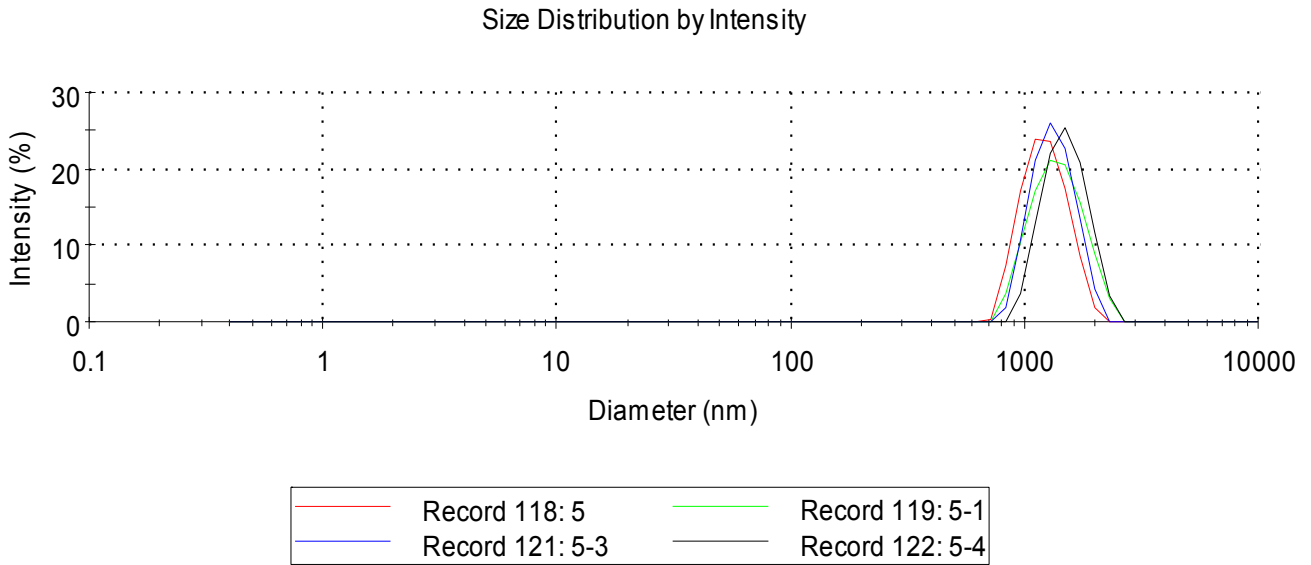**Size Distribution by Intensity**
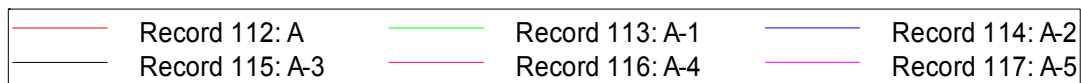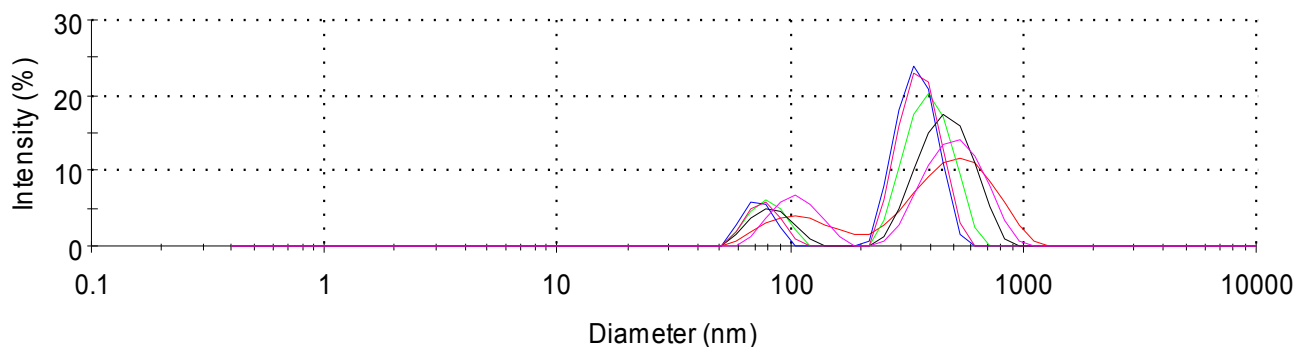
Appendix D-1.   Hydrodynamic diameter distribution of as-prepared samples

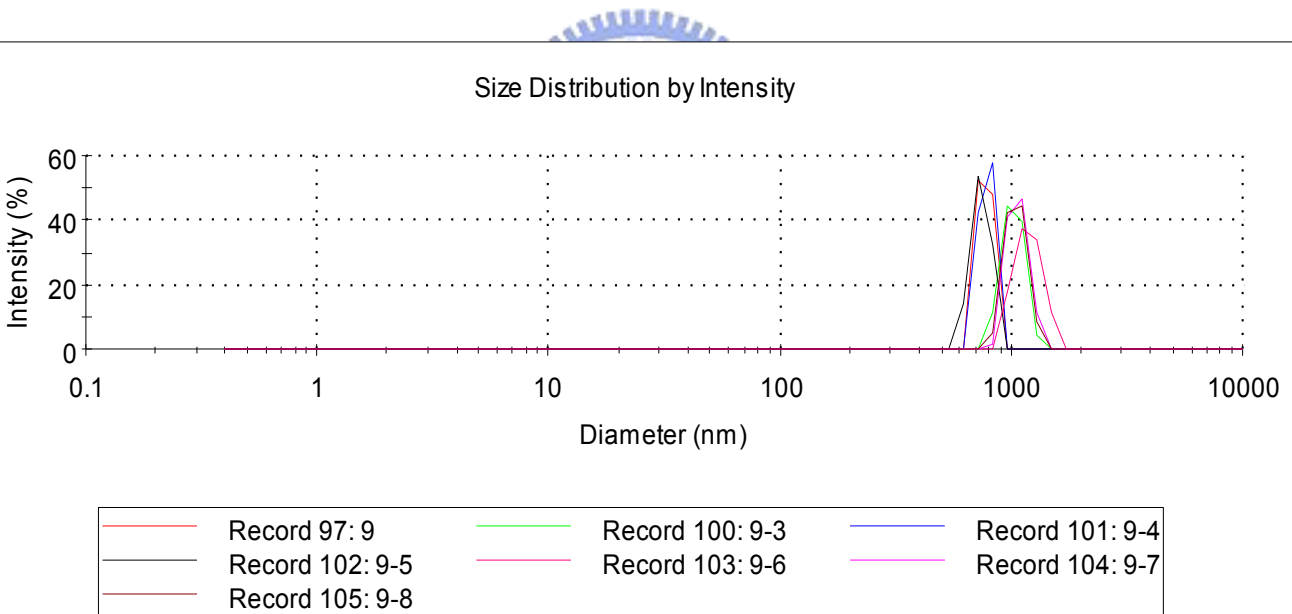**Size Distribution by Intensity**
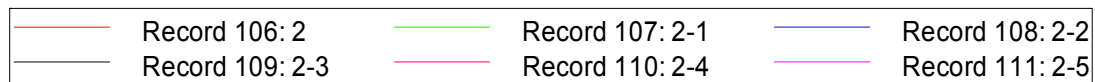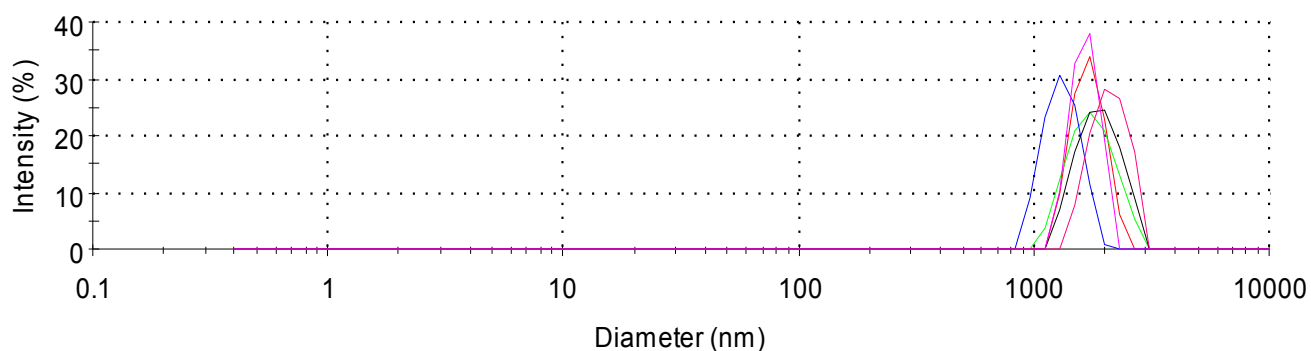
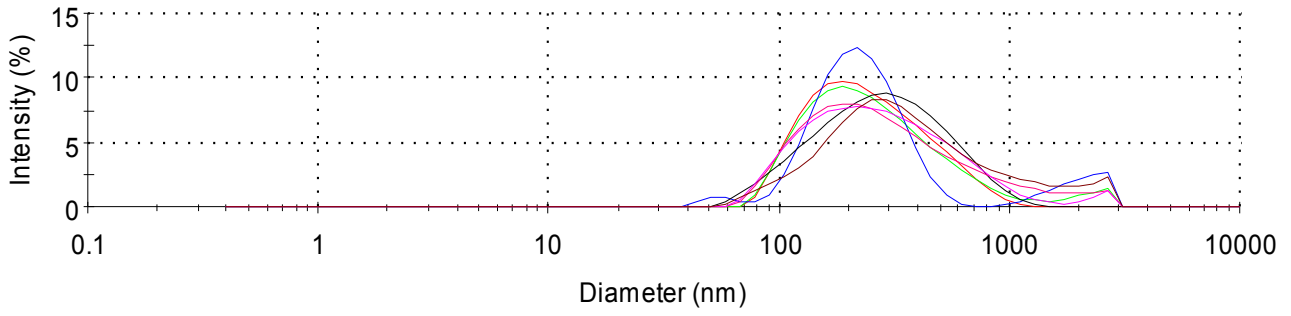Appendix D-2.   Hydrodynamic diameter distribution of samples calcined at 250 °C.

Size Distribution by Intensity

Legend:
- Record 118: 5
- Record 119: 5-1
- Record 121: 5-3
- Record 122: 5-4

Appendix D-3.   Hydrodynamic diameter distribution of samples calcined at 550 °C.

Size Distribution by Intensity

Legend:
- Record 97: 9
- Record 100: 9-3
- Record 101: 9-4
- Record 102: 9-5
- Record 103: 9-6
- Record 104: 9-7
- Record 105: 9-8

Appendix D-4.   Hydrodynamic diameter distribution of samples calcined at 950 °C.

Size Distribution by Intensity

|		
Record 123: P	Record 124: P-1	Record 125: P-2
Record 129: P-6	Record 131: P-8	Record 132: P-9
Record 133: P-10		

Appendix D-5.　Hydrodynamic diameter distribution of Degussa P25.

Appendix E.   Impregnation of P25 with phosphoric acid

Appendix E-1 presents the P(2p) high resolution XPS spectra of modified PP25-M. All the peaks are at binding energy of 133.6 to 133.9 eV which corresponds to P^{5+} of phosphate chemically bonded to surface of TiO_2. The area of P(2p) peaks apparently increases with the increase of concentration of phosphoric acid solution. The phosphated P25 powders are successfully synthesized via conventional pregnant method with different concentration of phosphoric acid.
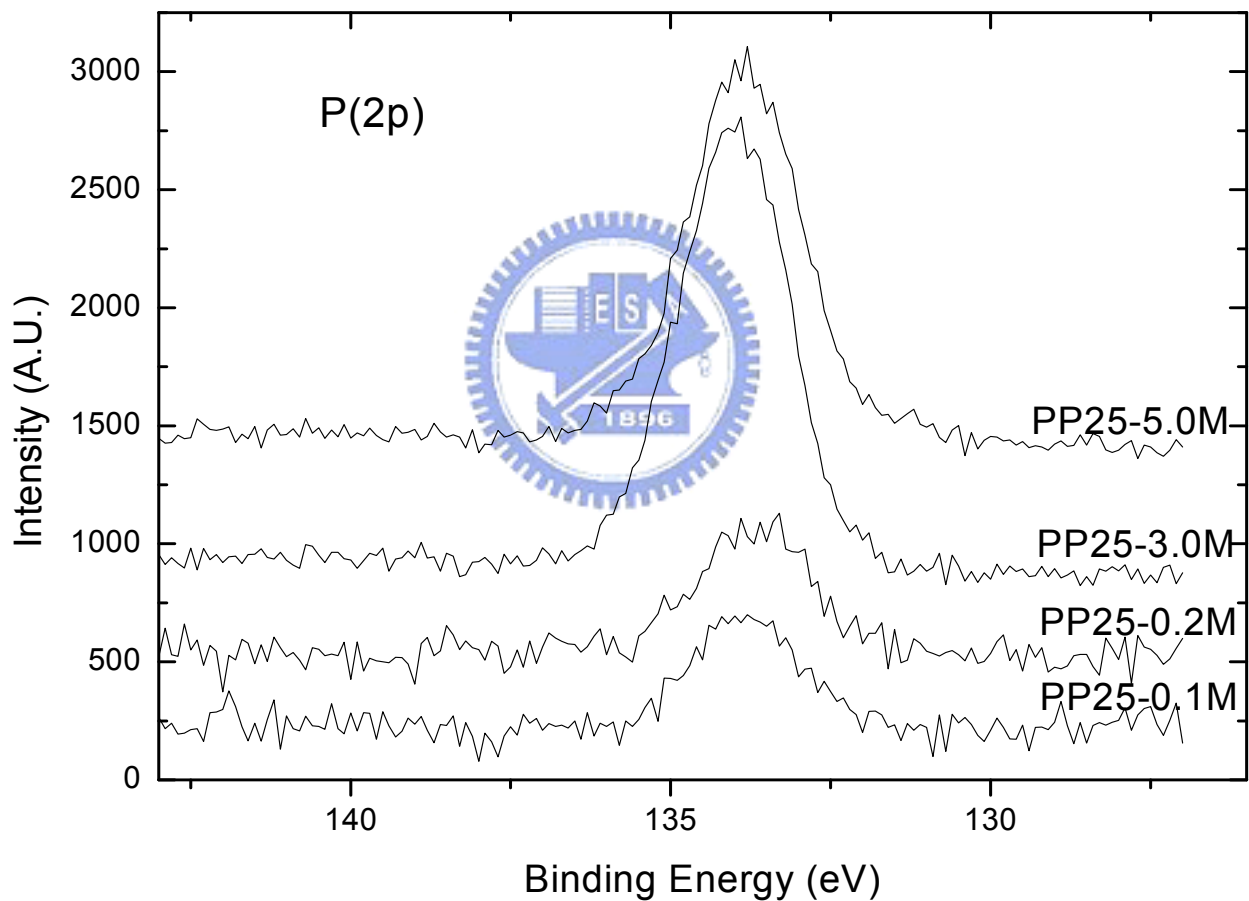

Appendix E-1. The evolution of P (2p) XPS spectra of P25 TiO_2 modified with different concentration of phosphoric acid.

Appendix E-2 displays the photocatalytic decoloration of RhB by P25 and PP25-M as a function of irradiation time at a wavelength of 305 nm and the surface P/Ti ratios are listed in Appendix E-3.   The degradation of RhB in the presence of photocatalysts indicates that each photocatalysts exhibited photocatalytic activity.   The photocatalytic degradation rate constants are ranked in the order of PP25-0.2M (k = 0.24 min^{-1}), PP25-0.1M (k = 0.23 min^{-1}), P25 (k = 0.14 min^{-1}), PP25-3.0M (k = 5.4×10^{-2} min^{-1}) and PP25-5.0M (k = 1.6×10^{-2} min^{-1}). Higher concentration of phosphoric acid for modification leads P25 having lower activity even than pure P25 dose.   This is similar with the observation by Korosi et al. that the photocatalytic activity of phosphated TiO$_2$ was related with the concentration of phosphate used and ratio of P/Ti from chemical analysis by ICP-AES.   In that study, the degradation rate first increased from P/Ti ratio of 0 to 0.01 and then decreased to a constant value with the increase of P content.   Higher content of phosphate were incorporated on surface layer as core-shell structure that the surface of TiO$_2$ was covered by phosphorous groups.

Since surface physicochemical properties influence much more on the photocatalytic reactions, the surface content of phosphorous as ratio of P/Ti was also examined.   Appendix E-4 presents the P/Ti ratio as a function of degradation rate constant of P25 and PP25-M. The degradation rate constant first increases and then decreases with the increase of surface P/Ti ratio.   The optimal value of surface P/Ti is around 0.63 and 0.72 for RhB degradation which give better activity than pure P25 or PP25 with higher surface P/Ti.   This phenomenon is similar to the observation by Korosi et al. though the total P/Ti was taken as the parameter.

Compared with PP25-M, Zr^{4+}/TiO$_2$ nano-crystals prepared in this study also presented similar surface content of P/Ti ratio of 0.58 indicating that the Zr^{4+}/TiO$_2$ nano-crystals have proper surface content of P/Ti ratio.
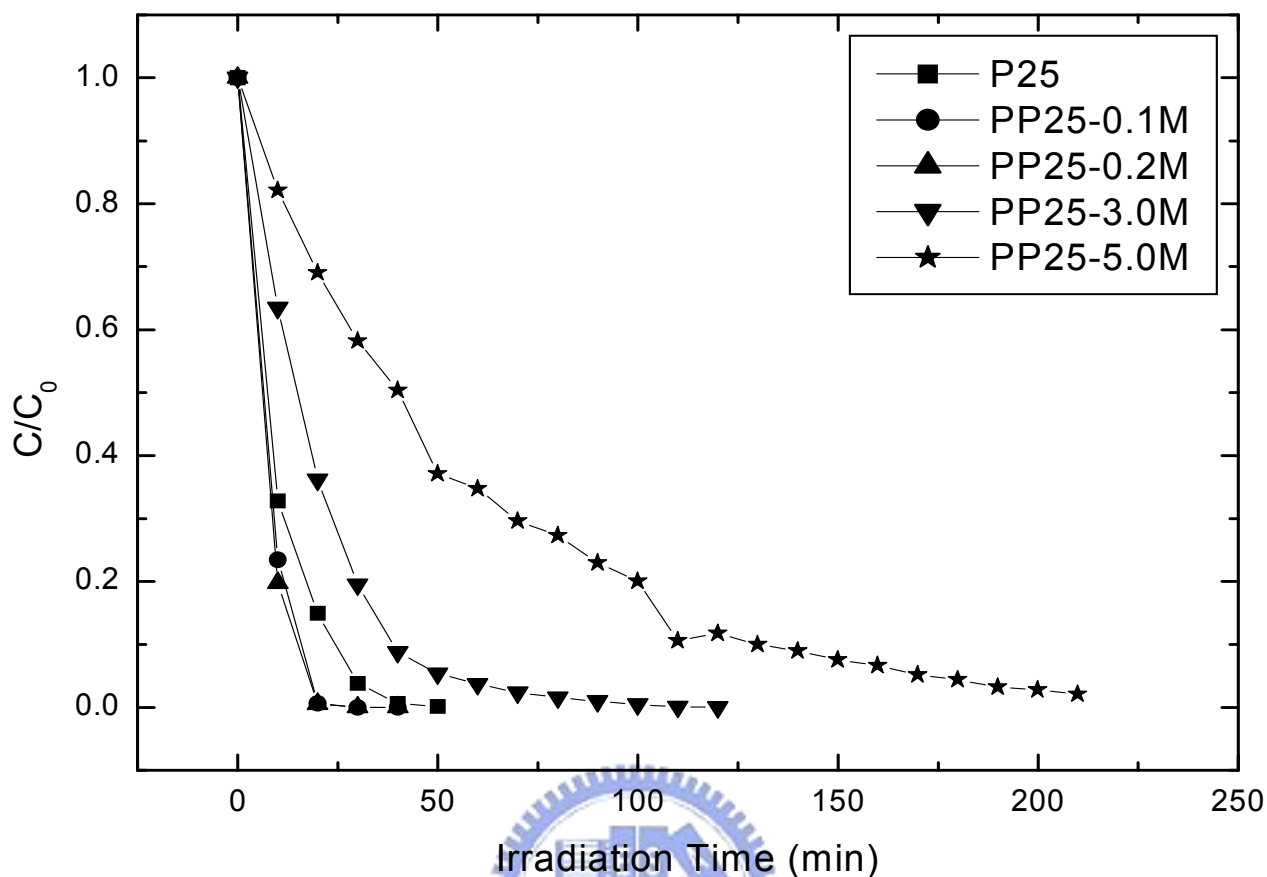
Appendix E-2.   The photobleaching acitvity of RhB by P25 and P25 modified with different

concentration of phosphoric acid.

Appendix E-3.   Photocatalytic activity of P25 and P25 modified with different concentration

of phosphoric acid on photobleaching of RhB.

Sample	P25	PP25-0.1M	PP25-0.2M	PP25-3.0M	PP25-5.0M
Surface P/Ti atomic ratio	0	0.63	0.72	0.95	1.28
Degradaiton rate constant (min^{-1})	0.14	0.23	0.24	5.4×10^{-2}	1.6×10^{-2}
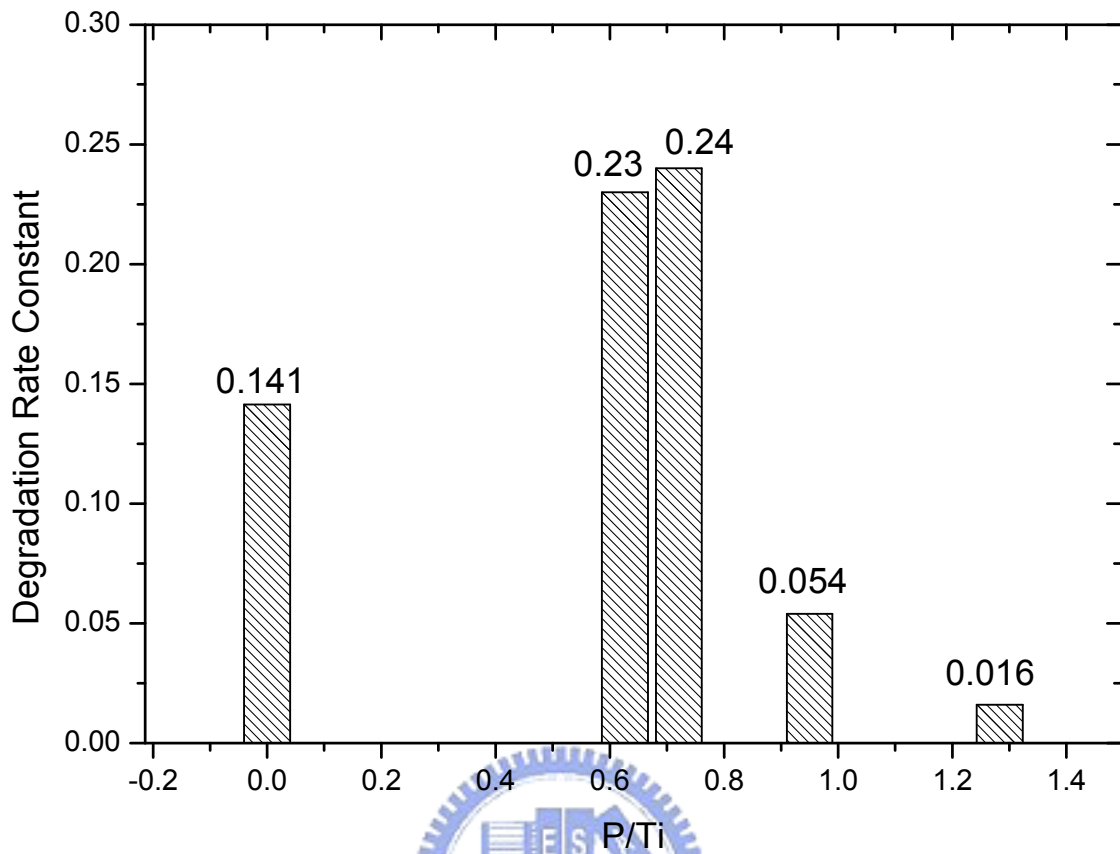
Appendix E-4.　Photobleaching of RhB dye on P25 with different surface phosphorous atomic ratio.